

Uncertainty quantification of a multi-component Hall thruster model at varying facility pressures.

Thomas A. Marks,^{1, a)} Joshua D. Eckels,¹ Gabriel E. Mora,¹ and Alex A. Gorodetsky^{1, b)}
Department of Aerospace Engineering, University of Michigan, Ann Arbor, Michigan, USA

(Dated: 14 July 2025)

Bayesian inference is applied to calibrate and quantify prediction uncertainty in a coupled multi-component Hall thruster model at varying facility background pressures. The model, consisting of a cathode model, discharge model, and plume model, is used to simulate two thrusters across a range of background pressures in multiple vacuum test facilities. The model outputs include thruster performance metrics, one-dimensional plasma properties, and the angular distribution of the current density in the plume. The simulated thrusters include a magnetically shielded thruster, the H9, and an unshielded thruster, the SPT-100. After calibration, the model captures several key performance trends with background pressure, including changes in thrust and upstream shifts in the ion acceleration region. Furthermore, the model exhibits predictive accuracy to within 10% when evaluated on flow rates and pressures not included in the training data, and the model can predict some performance characteristics across test facilities to within the same range. Evaluated on the same data as prior work [Eckels et al. 2024], the model reduced predictive errors in thrust and discharge current by greater than 50%. An extrapolation to on-orbit performance is performed with an error of 9%, capturing trends in discharge current but not thrust. Possible extensions and improvements are discussed in the context of using data for predictive Hall thruster modeling across vacuum facilities.

I. INTRODUCTION

Hall thrusters are the most widely-flown type of spacecraft propulsion system, but despite their popularity but they remain challenging to model. Predictive models—those which can accurately predict the plasma properties and global performance features of a thruster from geometry and operating conditions alone—are a longstanding goal of the Hall thruster modeling community. Unfortunately, poorly-understood physical effects have to date prevented such efforts from reaching fruition. In addition to the well-known problem of anomalous cross-field electron transport,¹ there are also many subtle and hard-to-model interactions between a thruster and the vacuum facility in which it is tested. These “facility effects” lead to thrusters performing differently in conditions attainable in on-ground facilities than they do in space.^{2–5} These effects complicate efforts to correlate ground test data with future in-space performance, increasing the expense of thruster development and qualification. In the absence of physics-based models for the aforementioned phenomena, engineering simulations of Hall thrusters rely on phenomenological models with parameters that must be calibrated to match data.^{6–9} These modeling choices introduce uncertainty which should be quantified.

To address this challenge, we apply a multidisciplinary modeling approach. We model the thruster-facility system in terms of a series of modular component models which interact via a limited set of coupling variables. We then apply Bayesian inference to calibrate our coupled model

against data. Once calibrated, we can make probabilistic predictions at operating conditions and facilities outside of those on which the model was trained. There are several advantages to this approach. First, the modularity allows new facility effects to be incorporated without significant changes to existing models. Additionally, models may be upgraded or replaced as improvements become available. Lastly, our approach places uncertainty quantification in a central role—as calibration is done probabilistically, we obtain not just point estimates but full distributions of model parameters and predictions of key quantities of interest (QoIs).

In our 2023 paper,¹⁰ we used an early version of this model to calibrate the SPT-100 thruster across background pressures. While we obtained promising initial results using the surrogate, predictive accuracy on held-out test data for the model itself was larger than 30% percent for certain quantities of interest and we did not faithfully capture all trends with pressure. Additionally, the model was only tested on a single thruster. We take several steps to address the limitations and outcomes of the prior work, and we extend the analysis to new thrusters and operating regimes. Specifically, we make the following changes: **1)** the computational expense of the thruster discharge model has been reduced by greater than 50%, which removes the need of a surrogate approximation for the UQ analysis, **2)** the Bayesian likelihood has been updated to limit over-confidence in learned model parameters, **3)** the pressure-dependent models for neutral ingestion, acceleration region shift, and plume divergence angle have been revised to better match experimental trends, and **4)** the anomalous transport model has been revised to increase its flexibility and generality across thrusters and datasets.

These changes, particularly the updates to our mod-

^{a)}Electronic mail: marksta@umich.edu

^{b)}Electronic mail: goroda@umich.edu

eling assumptions, resulted in a model that agrees with experimental data to within 10% for thrust and discharge current, with similarly low errors observed for the ion velocity, cathode coupling voltage, and plume ion current density. These results improve upon our previous work, in particular with respect to thrust and discharge current where the model test errors were 30 and 53%, respectively.¹⁰

Additionally, we expand the framework to simulate a magnetically-shielded thruster and demonstrate similar performance using less data. The low errors observed suggest that future work should be targeted toward the incorporation of additional QoIs and data sources. To that end, we highlight that the framework developed to support this model is flexible and able to incorporate new models and data sources for future model improvement activities, such as the inclusion of electrical or backscatter facility effects¹¹ or refined anomalous transport models.

This paper is organized as follows. First, in Sec. II, we describe the component models, the experimental data, and the methods we apply to calibrate the model. In Sec. III, we demonstrate that our coupled system model exhibits improved prediction accuracy and can extrapolate beyond its training dataset. Next in Sec. IV we comment on the applicability of our results to Hall thruster engineering design and consider ways to improve the extensibility of the model. Finally, in Sec. V, we summarize our findings.

II. METHODS

In this section, we describe the models in the coupled framework, the experimental data, the calibration procedure, and the uncertainty quantification approach.

A. Model

The Hall thruster system model, depicted in schematic form in Fig. 1, comprises an analytic cathode coupling model,¹² a one-dimensional fluid code for the main thruster discharge,¹³ and an analytic model for the expansion of the plume into a vacuum chamber.¹⁴ Together, these models predict five quantities of interest (QoIs): thrust, discharge current, cathode coupling voltage, spatially-resolved 1-D ion velocity, and the plume ion current density.

As illustrated in Fig. 1, each QoI arises from a different component model. The cathode model computes the cathode coupling voltage — the voltage needed to extract cathode electrons into the Hall thruster discharge plasma. This voltage determines the effective potential drop seen in the thruster model. The thruster model then predicts the uncorrected thrust, discharge current, ion current, and the 1-D axial spatial distribution of plasma properties within the thruster and near-field plume such as electron temperature and ion velocity. The ion current and thrust

then pass to the plume model, which predicts the angular distribution of the ion current density downstream of the thruster. The plume distribution can be analyzed to extract the divergence efficiency, which is used to correct the thrust. Each of the component models is given a functional dependence on the facility background pressure, enabling the coupled system to in principle capture a wide range of pressure-dependent phenomena.

The system model is defined as

$$\mathbf{y} = f(\mathbf{x}) = [f_1(\mathbf{x}), f_2(\mathbf{x}), \dots, f_Q(\mathbf{x})], \quad (1)$$

where \mathbf{x} and \mathbf{y} are vectors containing all model inputs and outputs, respectively and Q is the total number of QoIs (5 in this work). We further split the model inputs \mathbf{x} into *operating conditions* \mathbf{d} and *model parameters* $\boldsymbol{\theta}$. Operating conditions represent the experimental conditions at which the data were obtained. These may be known to within some inherent, irreducible uncertainty (*aleatoric uncertainty*) due to measurement precision or noise. In contrast, model parameters are unknown, model-specific, and have uncertainty that can be reduced by calibrating with data (*epistemic uncertainty*).

Both $\boldsymbol{\theta}$ and \mathbf{d} can be further broken down by component, with subscripts C , T and P denoting cathode, thruster, and plume respectively. Tabs. I and II provide the full list of each component's inputs and outputs, respectively. We use Bayesian inference, described further in Sec. II C, to calibrate the system against data and characterize the posterior distribution of the parameters $\boldsymbol{\theta}$. After calibrating, we use a Monte Carlo analysis of model predictions to understand the relative magnitudes of the aleatoric and epistemic uncertainties. This procedure is described further in Sec. II D.

1. Cathode coupling model

The cathode coupling model, developed in Ref. 12, predicts the cathode coupling voltage, V_{cc} , as a function of facility background pressure P_B using the following physically-derived relationship:

$$V_{cc} = V_{vac} + T_{ec} \log \left[1 + \frac{P_B}{P_T} \right] - \left[\frac{T_{ec}}{P_T + P^*} \right] P_B, \quad (2)$$

where V_{vac} is the expected coupling voltage at vacuum, T_{ec} is the effective cathode electron temperature, P^* is the pressure at which V_{cc} stops increasing, and P_T is the base pressure. These four quantities are treated as epistemic model parameters.

2. Thruster model

We use the open-source 1-D axial fluid Hall thruster code *HallThruster.jl*¹³ to model the thruster discharge. This code models a quasineutral, multi-species plasma of neutrals, ions, and electrons subject to an accelerating

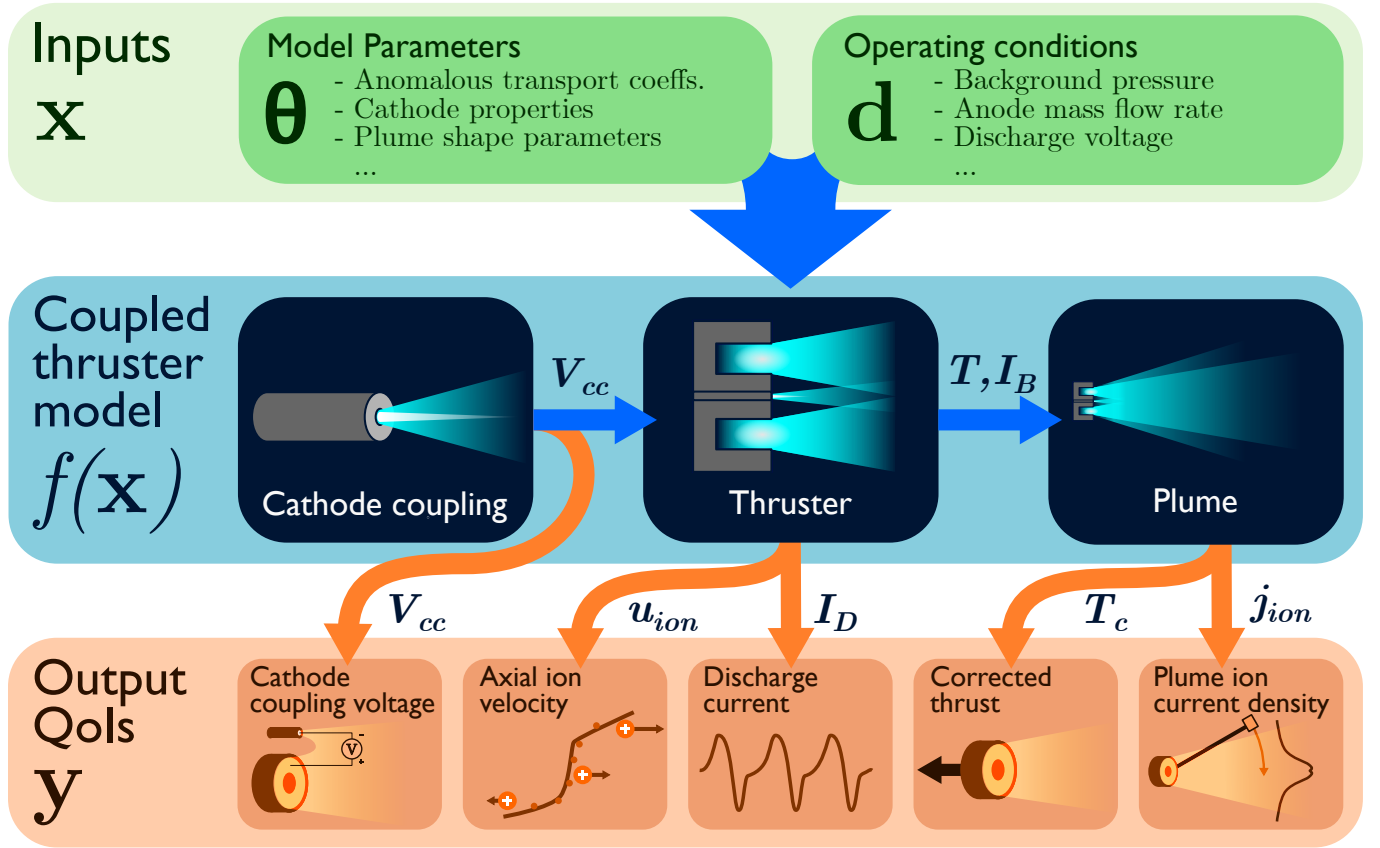


FIG. 1: Overview of the coupled Hall thruster system model, showing the connection between inputs, component models, and output QoIs. Input and output variables are defined in Tab. I and Tab. II, respectively.

TABLE I: Inputs to the coupled thruster-cathode-plume system. The abbreviations C, T, and P refer to the **C**athode, **T**hruster, and **P**lume component models, respectively.

Symbol	Description	Units	Components	Type	Distribution
V_d	Discharge voltage	V	C, T	Operating	$\mathcal{N}(\cdot, 2\%)$
P_B	Background pressure	Torr	C, T, P	Operating	$\mathcal{N}(\cdot, 5\%)$
\dot{m}_a	Anode mass flow rate	kg s^{-1}	T	Operating	$\mathcal{N}(\cdot, 2\%)$
T_{ec}	Cathode electron temperature	eV	C, T	Parameter	$\mathcal{U}(1, 6)$
V_{vac}	Vacuum coupling voltage	V	C	Parameter	$\mathcal{U}(0, 60)$
P_T	Base pressure	μTorr	C	Parameter	$\mathcal{U}(20, 200)$
P^*	Turning point pressure	μTorr	C	Parameter	$\mathcal{U}(1, 100)$
α_{anom}	Base inverse Hall parameter	-	T	Parameter	$\mathcal{U}(0, 1)$
β_{anom}	Anomalous transport barrier scale	-	T	Parameter	$\mathcal{U}(0, 1)$
z_{anom}	Anom. transport barrier location	-	T	Parameter	$\mathcal{U}(0.75, 1.5)$
L_{anom}	Anom. transport barrier width	-	T	Parameter	$\mathcal{U}(0, 0.5)$
Δz_{anom}	Anom. pressure axial shift scale	-	T	Parameter	$\mathcal{U}(0, 0.5)$
u_n	Neutral axial speed	m/s	T	Parameter	$\mathcal{U}(100, 500)$
c_w	Electron wall loss scale	-	T	Parameter	$\mathcal{U}(0.5, 1.5)$
f_n	Neutral ingestion scale	-	T	Parameter	$\mathcal{U}(1, 10)$
c_0	Ratio of main to scattered currents	-	P	Parameter	$\mathcal{U}(0, 1)$
c_1	Ratio of main to scattered div. angles	-	P	Parameter	$\mathcal{U}(0.1, 0.9)$
c_2	Slope of div. angle vs. pressure	rad Pa^{-1}	P	Parameter	$\mathcal{U}(-15, 15)$
c_3	Intercept of div. angle vs. pressure	rad	P	Parameter	$\mathcal{U}(0.2, \pi/2)$
$c_4 (10^x)$	Slope of neutral density vs. P_B	$\text{m}^{-3} \text{Pa}^{-1}$	P	Parameter	$\mathcal{U}(18, 22)$
$c_5 (10^x)$	Intercept of neutral density vs. P_B	m^{-3}	P	Parameter	$\mathcal{U}(14, 18)$

$\mathcal{U}(x, y)$ denotes a uniform distribution between x and y .

$\mathcal{N}(\cdot, x\%)$ denotes a normal distribution about a nominal value with a standard deviation of $x\%$.

Variables with the (10^x) notation denote a log-uniform distribution.

TABLE II: Outputs of the coupled cathode-thruster-plume system.

Symbol	Description	Units	Component	Coupling
V_{cc}	Cathode coupling voltage	V	Cathode	Cathode–Thruster
T	Uncorrected thrust	N	Thruster	Thruster–Plume
I_B	Ion current	A	Thruster	Thruster–Plume
I_D	Discharge current	A	Thruster	-
u_{ion}	Axial singly-charged ion velocity	m/s	Thruster	-
T_c	Corrected thrust	N	Plume	-
j_{ion}	Plume ion current density	A/m ²	Plume	-

potential. HallThruster.jl models neutrals using a continuity equation and solves both continuity and momentum equations for ions. The code assumes electrons are an inertialess fluid and computes the electrostatic potential and electron current density using charge conservation and the generalized Ohm's law / quasineutral drift diffusion approximation.^{7,15} It then solves a transport equation for the electron temperature. Up to three ion charge states can be included; we consider only singly-charged ions in the present work. HallThruster.jl uses V_{cc} calculated by cathode coupling model as the electric potential at the right (cathode) boundary. The model outputs thrust and ion current, which are passed as inputs to the plume model, as well as discharge current and many spatially-resolved plasma properties, including the axial ion velocity.

HallThruster.jl cannot self-consistently resolve instability-induced cross-field electron transport (a problem inherent in all fluid Hall thruster models). Instead, one must specify a spatially-varying profile for the so-called “anomalous” electron collision frequency. These are often piecewise-linear functions of space.^{7,9} We employ in this work a four-parameter model of the following form:

$$\Omega_{anom}^{-1} = \alpha_{anom} \left(1 - \beta_{anom} \exp \left[- \left(\frac{\hat{z} - z_{anom}}{L_{anom}} \right)^2 \right] \right) \quad (3)$$

where $\Omega_{anom} = \omega_{ce}/\nu_{anom}$ is the anomalous electron Hall parameter, ν_{anom} is the anomalous electron collision frequency, ω_{ce} is the electron cyclotron frequency, and \hat{z} is the axial coordinate normalized by the discharge channel length. The transport obeys the Bohm scaling ($\nu_{anom} \sim \omega_{ce}$) with a localized reduction in transport following a Gaussian profile at a specified location. This form captures key features seen in calibrated piecewise-linear profiles⁹ while keeping the number of parameters low. The reduction in transport increases the peak electric field, producing the steep ion acceleration profiles observed in experimental data. The parameters of this model— α_{anom} , β_{anom} , z_{anom} , and L_{anom} —represent the maximum inverse Hall parameter and the scale, location, and width of the transport barrier, respectively. The latter two parameters are non-dimensionalized by the discharge channel length to increase the transportability of parameters between thrusters. We chose this parameterization so that each parameter is of the order $\mathcal{O}(1)$ and to provide a high degree of interpretability.

As given, this model has no pressure dependence and thus would be unable to capture the observed upstream shift in the ion acceleration region in response to increasing back-pressure¹⁶. To account for this, we introduce a phenomenological model for this displacement:

$$\Delta z(P_B) = \Delta z_{anom} L_{ch} \left(\frac{1}{1 + e^{-2(P_B/P_0 - 1)}} - \frac{1}{1 + e^2} \right), \quad (4)$$

where P_B is the background pressure and $\Delta z(P_B)$ describes the magnitude of the upstream shift. The param-

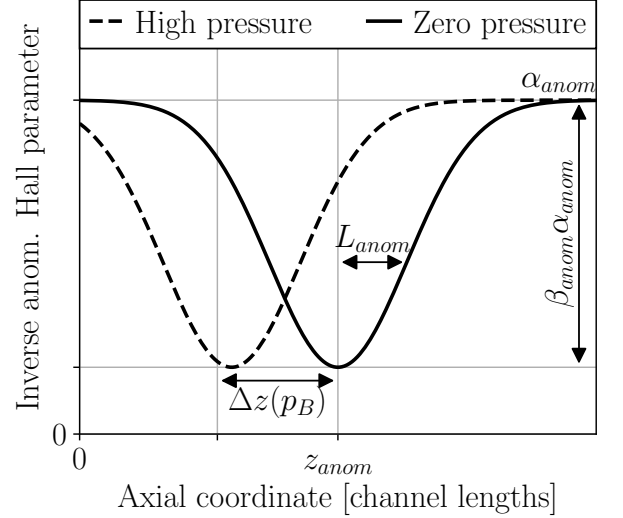


FIG. 2: Notional plot of the anomalous electron transport model used in this work, illustrating the key parameters in Eq. (3) and the pressure shift from Eq. (4).

eters of this model are Δz_{anom} and P_0 , which describe the magnitude of the shift and the center of the shift with respect to background pressure. Eq. (4) takes the form of a logistic curve, which captures the intuition that the anomalous transport profile should not move arbitrarily far up- or down-stream as background pressure approaches large or small values. In practice, we have found that setting $P_0 = 25 \times 10^{-6}$ Torr shows good agreement to data for several thrusters, so we leave only Δz_{anom} as a free parameter. This model is implemented by setting $z = z_0 + \Delta z(p_B)$ in Eq. (3), where z_0 is the un-shifted axial position. We show in Fig. 2 the shape of the transport model and the effect of the pressure shift on the electron transport curve.

We calibrate two additional parameters in addition to those controlling anomalous transport: a neutral ingestion scale factor f_n and a wall loss scale factor c_w . Hall thrusters typically exhibit increased thrust at high background pressures in part due to the ingestion of background neutrals, which serve as extra propellant.^{17,18} We calculate the amount of ingested neutral propellant as the one-sided flux of a stationary Maxwellian population of neutrals of a specified background pressure and temperature across the exit plane of the thruster. On its own, this model is known to severely under-predict the true degree of neutral ingestion,¹⁸ so we multiply the ingested neutral flux by f_n to better match experiments. Second, the wall loss scale parameter, c_w , scales the assumed edge-to-center density ratio from its base value of 0.5 when performing electron sheath loss calculations. These wall losses are the main method by which HallThruster.jl distinguishes between magnetically-shielded thrusters like

the H9 and unshielded thrusters like the SPT-100. In shielded thrusters, we assume the wall temperature equals the anode temperature and we disallow ion wall losses, while in unshielded thrusters, the wall temperature equals the channel average temperature and ion wall losses are accounted for.

All simulations in this work use a uniform grid of 100 cells and a domain length of three thruster channel lengths. We simulate one millisecond of thruster operation and average all QoIs over the last 500 microseconds of the simulation. With these settings, a single `HallThruster.jl` simulation takes about six seconds on a single core of an Intel Xeon Gold 6154 CPU (the exact time varies per-run due to adaptive time-stepping).

To summarize, the thruster model presented here differs from our previous work¹⁰ in a few key aspects: the anomalous transport and pressure shift models are more expressive, and we have included additional wall loss and neutral ingestion parameters. In principle, these changes should allow the model to better capture observed trends in facility effects and to better generalize over operating conditions. Additionally, a combination of internal code optimizations and coarsened grid resolution has reduced the runtime by nearly a factor of ten, making it practical to perform Bayesian inference directly on the model without a surrogate. To assess the impact of the modeling changes from the inference changes, we report in Appendix B results obtained by calibrating the model of our previous work using the inference procedure of the present work.

3. Plume model

We employ the semi-empirical plume expansion model used in Refs. 10 and 14. This model treats the ion current density in the plume (j_{ion}) as composed of three populations — main beam ions, ions scattered by inelastic collisions, and slow ions produced by charge-exchange collisions with neutrals:

$$j_{\text{ion}} = j_{\text{beam}} + j_{\text{scatter}} + j_{\text{cex}}. \quad (5)$$

The first two populations follow Gaussian angular distributions with their own characteristic divergence angles, while the latter expands uniformly in a hemisphere. The current density of each population decays proportionally to the inverse square of the distance from the thruster exit plane.

Given the current density $j_{\text{ion}}(r, \phi)$ as a function of distance r from the thruster exit plane and angle ϕ from thruster centerline, we compute the beam divergence angle ϕ_d from the ratio of the axial and total ion beam currents:¹⁹

$$\phi_d = \frac{I_{B,z}}{I_B} = \frac{2\pi r^2 \int_0^{\pi/2} j_{\text{ion}}(r, \phi) \cos(\phi) \sin(\phi) d\phi}{\int_0^{\pi/2} j_{\text{ion}}(r, \phi) \cos(\phi) d\phi}. \quad (6)$$

Here, $\phi = 0$ indicates the thruster centerline. We then “correct” the thrust from the thruster model ($T \rightarrow T_c$) according to

$$T_c = T \cos(\phi_d), \quad (7)$$

which accounts for the loss in axially-directed thrust due to beam divergence. This differs from our previous work,¹⁰ in which we used the “uncorrected” thrust directly and consequently over-predicted the true measured thrust.

B. Experimental data

We study two thrusters in this paper — the SPT-100 and the H9. The SPT-100, shown in Fig. 3a, is a widely-tested 1.5 kW-class Hall thruster developed by Fakel in Russia.¹⁷ Due to its age and the availability of its geometry and magnetic field configuration, it is often used for model development activities. The H9 (Fig. 3b) is a magnetically-shielded 9 kW-class Hall thruster developed in collaboration between the University of Michigan (UM), the Air Force Research Laboratory and the Jet Propulsion Laboratory.²⁰

We summarize the experimental datasets used in this study for both thrusters in Tab. III, including the measurement QoIs, the number of unique operating conditions (sets of V_d, P_B, \dot{m}_a) in each dataset, and the original sources of the data. Datasets categorized as “training” are used in the calibration procedure to tune the model parameters. We additionally include “test” datasets which are not seen during training; we use these to assess how well the model generalizes beyond the training data. The SPT-100 datasets^{16,17,21} were all obtained using Xenon propellant, and all H9 datasets used Krypton.^{22,23}

The SPT-100 datasets from Ref. 21 include performance measurements (i.e. coupling voltage, thrust, and discharge current) and angularly-resolved measurements of the ion current density in the plume at a radius of one meter from the thruster exit plane, comprising fifteen total operating conditions across two facilities (L3-Harris and Aerospace Corporation). The additional training dataset from Ref. 16 includes the discharge current and spatially-resolved axial ion velocity at three conditions. The test dataset from Ref. 17, includes global performance metrics (thrust and discharge current) at a diverse range of flow rates and background pressures. Finally, the SPT-100 test dataset from Ref. 3 contains measurements from two Russian Express-A satellites, both on the ground and on-orbit. The thruster ran at 300 V on the ground and 310 V on orbit. The mass flow rate for the on-orbit data was not measured and was instead estimated by the authors based on previous SPT-100 experiments; this makes using the data somewhat challenging, as mass flow rate has a large effect on both thrust and discharge current, and often varies with background pressure if a fixed discharge current is maintained. We use the estimated value for the flow rates in this study, but note that larger uncertainty bounds on the flow rate could have been included to

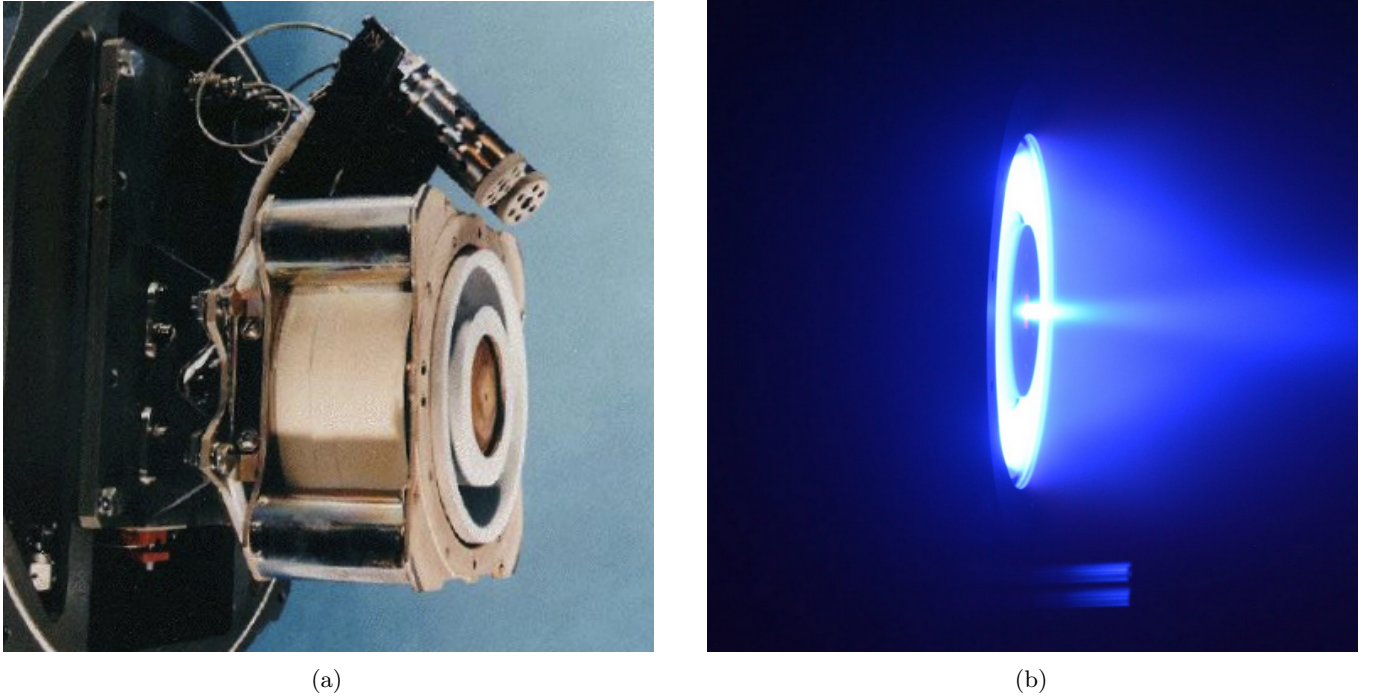


FIG. 3: (a) The SPT-100 Hall thruster. (b) The H9 Hall thruster operating on Krypton in the Large Vacuum Test Facility at the University of Michigan.

TABLE III: Summary of the experimental training and test datasets for the SPT-100 and H9 thrusters in this study. The measurement quantities of interest (QoIs) are listed along with the number of unique operating conditions (sets of V_d, P_B, \dot{m}_a) for each dataset.

Thruster	Summary	Ref.	QoIs	Conditions	Category
SPT-100	Diamant et al. 2014, L3	21	$V_{cc}, I_D, T_c, j_{ion}$	8	Training
SPT-100	Diamant et al. 2014, Aerospace Corp.	21	V_{cc}, I_D, T_c	7	Training
SPT-100	Macdonald-Tenenbaum et al. 2019	16	I_D, u_{ion}	3	Training
SPT-100	Sankovic et al. 1993	17	I_D, T_c	119	Test
SPT-100	Manzella et al. 2001	3	I_D, T_c	2	Test
H9	UM 2024, Plume	23	V_{cc}, I_D, j_{ion}	3	Training
H9	UM 2024, Velocity	22	I_D, u_{ion}	5	Training
H9	GT 2024	24	I_D, T_c, j_{ion}	3	Test

Nomenclature for the QoIs is provided in Tab. II.

account for this lack of information. We include details on this dataset in Appendix A.

The H9 data in Tab. III originates from a 2024 test campaign to compare the performance of the same thruster at two different test facilities, namely Vacuum Test Facility 2 at the Georgia Institute of Technology (GT) and the Large Vacuum Test Facility at the University of Michigan. The UM data²² spans eight background pressures: five of these conditions (the “velocity” dataset in Tab. III) include laser-induced fluorescence measurements of ion velocity²² and three (the “plume” dataset) contain both cathode coupling voltage and plume ion current density measurements at radii of 1.16 m, 1.32 m, 1.32 m, and 1.64 m.²³ The GT data²⁴ contains three operating conditions, again differing mainly in background pressure, and

includes thrust, ion current density measurements at a distance of one meter, and discharge current. For all H9 datasets, the thruster operated at a nominal discharge current of 15 A and a discharge voltage of 300 V.

C. Calibration procedure

We calibrate the epistemic model parameters θ against experimental data using a Bayesian approach. We use Markov Chain Monte Carlo (MCMC) to generate samples of the epistemic parameters according to their posterior distribution, which is given by Bayes’ rule:

$$p(\theta | \mathbf{y}_e) = \frac{1}{Z} p(\mathbf{y}_e | \theta) p(\theta),$$

where \mathbf{y}_e is a vector of all experimental data at all operating conditions, $p(\boldsymbol{\theta} | \mathbf{y}_e)$ is the posterior distribution of all the epistemic parameters, $p(\mathbf{y}_e | \boldsymbol{\theta})$ is the likelihood of the experimental data given some fixed set of parameters and the model, $p(\boldsymbol{\theta})$ is the prior distribution representing the state of knowledge about the model parameters prior to observing any data, and Z is a normalizing constant. For simplicity, we have assumed no aleatoric uncertainty in the operating conditions \mathbf{d} during calibration, i.e. we calibrate the epistemic model parameters $\boldsymbol{\theta}$ assuming exact operating conditions. The prior distributions for each parameter are listed in Tab. I, where we have used uninformative uniform distributions over the expected ranges for each parameter and we assume all parameters are independent.

To obtain the likelihood, we assume the measurement noise of each observation of each quantity of interest is independent. For each QoI, n_q represents the number of operating conditions which have data for that QoI, and m_q is the length of the observation of that QoI. For thrust, $m_q = 1$ since we only observe a single thrust per condition, but for ion velocity or ion current density m_q may be 10 or greater since we have many ion velocity measurements at each condition.

$$p(\mathbf{y}_e | \boldsymbol{\theta}) = \prod_{q=1}^Q p(\mathbf{y}_{eq} | \boldsymbol{\theta}) = \prod_{q=1}^Q \prod_{j=1}^{n_q m_q} p(y_{eq}^{(j)} | \boldsymbol{\theta}),$$

where $y_{eq}^{(j)}$ represents the j -th observation of the q -th QoI and Q is the number of QoIs. The outer product assumes independence across quantities of interest, and the inner product assumes independent observations within and across an operating conditions. We next assume that the error can be modeled using additive Gaussian noise. Next, we need to assume some form of error model between the observed model and the predicted value. Specifically, we model the predicted observation of the q -th QoI at the j -th operating condition as

$$y_{eq}^{(j)} = f_q(\boldsymbol{\theta}, \mathbf{d}_{eq}^{(j)}) + \xi_q, \quad \xi_q \sim \mathcal{N}(0, \sigma_q^2).$$

where $\mathbf{d}_{eq}^{(j)}$ represents the operating conditions associated with a specific experimental data point, ξ_q represents a stochastic model for the error between the model prediction and the observation, and σ_q^2 is the variance of this error, chosen per-QoI. Under this model we have

$$p(y_{eq}^{(j)} | \boldsymbol{\theta}) = \mathcal{N}(f_q(\boldsymbol{\theta}, \mathbf{d}_{eq}^{(j)}), \sigma_q^2).$$

The log-likelihood is then

$$\log p(\mathbf{y}_e | \boldsymbol{\theta})$$

$$\begin{aligned} &= \sum_{q=1}^Q \sum_{j=1}^{n_q m_q} -\log \left(\sqrt{2\pi} \sigma_q \right) - \frac{\left(y_{eq}^{(j)} - f_q(\boldsymbol{\theta}, \mathbf{d}_{eq}^{(j)}) \right)^2}{2\sigma_q^2} \\ &= \sum_{q=1}^Q \left[-n_q m_q \log \left(\sqrt{2\pi} \sigma_q \right) - \sum_{j=1}^{n_q m_q} \frac{\left(y_{eq}^{(j)} - f_q(\boldsymbol{\theta}, \mathbf{d}_{eq}^{(j)}) \right)^2}{2\sigma_q^2} \right] \end{aligned}$$

As only the second term depends on $\boldsymbol{\theta}$, we can fold the summation over the first term into a constant C which drops out during MCMC sampling or optimization, giving

$$\log p(\mathbf{y}_e | \boldsymbol{\theta}) = -\frac{1}{2} \sum_{q=1}^Q \frac{1}{\sigma_q^2} \sum_{j=1}^{n_q m_q} \left(y_{eq}^{(j)} - f_q(\boldsymbol{\theta}, \mathbf{d}_{eq}^{(j)}) \right)^2 + C.$$

As written, this likelihood over-weights QoIs like ion velocity which have tens of points per operating condition and underweight global properties like thrust. To mitigate this, we express the pointwise standard deviation σ_q in terms of an average *relative* error across a whole dataset:

$$\sigma_q^2 = c_q \gamma_q^2,$$

where γ_q represents a relative measurement error and c_q is a reference magnitude. We use the data to set c_q based on the squared L-2 norm of the vector of observations of q , averaged over the number of operating conditions in which q was observed:

$$\sigma_q^2 = \frac{\|\mathbf{y}_{eq}^{(j)}\|^2}{n_q} \gamma_q^2,$$

where the $\|\mathbf{y}_{eq}\|^2 = \sum_j^{m_q n_q} (y_{eq}^{(j)})^2$. Using this choice, the log likelihood becomes

$$\log p(\mathbf{y}_e | \boldsymbol{\theta}) = -\frac{1}{2} \sum_{q=1}^Q \frac{n_q}{\gamma_q^2} \frac{\|\mathbf{y}_{eq} - f_q(\boldsymbol{\theta}, \mathbf{d}_{eq})\|^2}{\|\mathbf{y}_{eq}\|^2} + C. \quad (8)$$

The interpretation of $\gamma_q/\sqrt{n_q}$ is as an averaged relative L-2 norm of the difference between the data and the model output in QoI q across all operating conditions. In the results that follow we choose $\gamma_q/\sqrt{n_q} = 2.5\%$ for all quantities of interest, which is equal to or lower than to the estimated relative measurement error for all quantities except the cathode coupling voltage and thrust of the SPT-100. For these we instead set $\gamma_q/\sqrt{n_q} = 1\%$, which is closer to the experimental error for these quantities on this thruster.

With this likelihood in hand, we employ MCMC (specifically the Delayed Rejection Adaptive Metropolis algorithm²⁵) to draw 50,000 samples from the posterior distribution. As the Markov chain takes time to arrive at the true posterior distribution, we discard the first half of the drawn samples and perform our analysis using the second half. We calibrate each thruster separately, giving each its own posterior parameter distribution. We note that this likelihood differs somewhat from that used in our previous paper¹⁰. To assess the impact of this change, independent of differences in our modeling assumptions and parameterizations, we report in Appendix B results from our previous model using the new likelihood which can be compared with the results obtained in the following sections.

D. Uncertainty quantification

After obtaining samples from the posterior parameter distribution, we then quantify the uncertainty in model predictions when comparing to experimental data. We wish to characterize the impact of both epistemic and aleatoric uncertainty in our predictions: the epistemic uncertainty is obtained by propagating only samples of model parameters θ through the model, and total uncertainty (aleatoric + epistemic) is obtained by sampling the aleatoric uncertainties in the operating conditions \mathbf{d} . The epistemic and aleatoric uncertainties are assumed independent, and therefore this approach provides the total uncertainty. In decomposing the epistemic and aleatoric uncertainties in this way, we slightly underestimate the true epistemic uncertainty but significantly simplify the calibration and analysis.

Concretely, we adopt the following procedure. For epistemic uncertainty, we draw N samples from the posterior parameter distribution $p(\theta | \mathbf{y}_e)$ obtained by MCMC (we take $N = 1000$ throughout our analysis), keeping the aleatoric variables at their nominal values. For the total uncertainty, we draw N samples from both $p(\theta | \mathbf{y}_e)$ and $p(\mathbf{d})$ (the prior distribution of the aleatoric variables, as given in Tab. I). In both cases, we then evaluate the model at each input vector $\mathbf{x} = (\theta, \mathbf{d})$ and compute statistics (such as the mean and variance) on the model outputs. Unless otherwise noted, we present in our results the median prediction of each QoI as well as a 90% credible interval of predictions drawn from both distributions. The difference between the epistemic uncertainty bands and the total uncertainty bands shows the impact of aleatoric uncertainty compared to epistemic uncertainty.

III. RESULTS

In this section, we first examine the parameter distributions obtained by the calibration procedure, then we show the performance on training datasets, and finally we validate the model's generalization on the independent test datasets, including a preliminary extrapolation of the SPT-100 data to orbit.

A. Calibration

In this section, we present the results of the Bayesian inference procedure described in Sec. II C. We list for the SPT-100 and H9, respectively in Tabs. IV and V, each calibration parameter, their prior distributions, and several statistics of their posterior (post-calibration) distributions. We include plots of the marginal posterior parameter distributions for each component model in Appendix C.

We find that the posterior distributions of most parameters are narrowed significantly from the prior distributions, indicating that the data was informative for reducing the

epistemic uncertainty while not being so narrow as to be point estimates. There are a few parameters, however, whose posterior distributions span nearly the same range as their priors:

1. **The wall loss scale parameter (c_w) for the H9:** The wall loss model's behavior for shielded thrusters described in Sec. II A 2 reduces the wall interactions to the point that c_w has little effect on the overall discharge.

2. **The neutral ingestion scale parameter (f_n) for both thrusters:** This indicates that the thermal model of neutral ingestion is inadequate, even with a scaling factor that can amplify the effect of background pressure.

3. **Cathode parameters (especially T_{ec} and P_T) for the SPT-100:** The closeness of the cathode data to a flat line at $V_{cc} = V_{vac}$ meant we were not able to significantly reduce the uncertainty in these parameters.

4. **The neutral ingestion scale parameter (f_n) for the SPT-100:** While this parameter was intended to improve the model's sensitivity to changing background pressure, in practice it was not able to be inferred with precision. Instead, the coupling between thruster and plume models meant that increased plume divergence at lower pressure was sufficient to replicate the trends in the thrust data.

Additionally, some parameters differed between thrusters. The median value of the anomalous pressure shift parameters, Δz_{anom} , was nearly twice as high for the SPT-100 than for the H9, accurately reflecting the difference in the magnitude of the upstream acceleration shift with background pressure observed in the two thrusters' training datasets. Similarly, the overall anomalous collision frequency scale, α_{anom} was twice as high for the H9 as for the SPT-100, although for both thrusters it varied across at least a factor of two. Finally, c_2 , which determines how the divergence angle trends with background pressure was found to have an opposite sign for the H9 as in the SPT-100. For the SPT-100, it is uniformly negative, indicating a reduction in plume divergence at high pressure. By contrast, for the H9 the median value is positive, leading to the opposite trend. These inferred parameters reflect real trends in the data, and indicate the success of the calibration procedure.

1. SPT-100

In Figs. 4, 5, and 6, we show how the model predictions of cathode coupling voltage, discharge current, and thrust differ under the prior parameter distribution and the calibrated posterior distribution. In these plots, we show the median model output of each QoI and the 90% credible interval (CI). The confidence interval contains both aleatoric and epistemic uncertainties in the prior plots, while in the posterior plots we show both separately. For each QoI, the uncertainty is dramatically reduced under

TABLE IV: Statistics of the 1-D marginal posteriors of the SPT-100 parameters.

Variable	Prior	Posterior					
		Min	5 th pctile	50 th pctile	95 th pctile	Max	Std dev
P_T	$\mathcal{U}(10, 100)$	10	14.47	48.72	93.63	99.95	24.81
P^*	$\mathcal{U}(10, 200)$	10.04	25.60	64.85	140.12	197.95	35.27
T_e	$\mathcal{U}(1, 6)$	1	1.17	2.92	4.85	6	1.18
V_{vac}	$\mathcal{U}(0, 60)$	29.84	30.87	31.75	32.40	32.88	0.46
β_{anom}	$\mathcal{U}(0, 1)$	0.95	0.97	0.99	1	1	0.01
z_{anom}	$\mathcal{U}(0.75, 1.5)$	1	1.06	1.14	1.20	1.26	0.04
α_{anom}	$\mathcal{U}(0, 1)$	0.02	0.04	0.06	0.09	0.10	0.01
Δz_{anom}	$\mathcal{U}(0, 0.5)$	0.08	0.20	0.33	0.45	0.5	0.08
L_{anom}	$\mathcal{U}(0, 0.5)$	0.25	0.34	0.43	0.49	0.5	0.05
c_w	$\mathcal{U}(0.5, 1.5)$	0.5	0.51	0.67	1.25	1.50	0.23
f_n	$\mathcal{U}(1, 10)$	1	1.40	5.23	9.53	10	2.59
u_n	$\mathcal{U}(100, 500)$	157.59	195.57	278.11	378.17	448.28	55.07
c_0	$\mathcal{U}(0, 1)$	0.67	0.71	0.76	0.79	0.82	0.03
c_1	$\mathcal{U}(0.1, 0.9)$	0.26	0.29	0.32	0.36	0.41	0.02
c_2	$\mathcal{U}(-15, 15)$	-15	-14.52	-12.36	-8.88	-5.32	1.77
c_3	$\mathcal{U}(0.2, \pi/2)$	0.2	0.2	0.21	0.22	0.24	0.01
c_4 (10^x)	$\mathcal{U}(18, 22)$	20.02	20.15	20.33	20.45	20.55	0.10
c_5 (10^x)	$\mathcal{U}(14, 18)$	14	14.03	14.33	15.48	16.88	0.50

Variables with the (10^x) notation indicate a log-uniform distribution.

TABLE V: Statistics of the 1-D marginal posteriors of the H9 parameters

Variable	Prior	Posterior					
		Min	5 th pctile	50 th pctile	95 th pctile	Max	Std dev
P_T	$\mathcal{U}(1, 100)$	1	1.22	3.18	10.89	40.03	3.51
P^*	$\mathcal{U}(10, 200)$	41.24	42.47	45.33	46.86	48.79	1.33
T_e	$\mathcal{U}(1, 6)$	3.03	4.18	5.4	5.95	6	0.57
V_{vac}	$\mathcal{U}(0, 60)$	17.44	18.50	21.94	26.47	30	2.49
β_{anom}	$\mathcal{U}(0, 1)$	0.94	0.96	0.98	0.99	1	0.01
z_{anom}	$\mathcal{U}(0.75, 1.5)$	1	1.04	1.07	1.1	1.15	0.02
α_{anom}	$\mathcal{U}(0, 1)$	0.04	0.07	0.13	0.18	0.21	0.03
Δz_{anom}	$\mathcal{U}(0, 0.5)$	0.01	0.06	0.18	0.29	0.37	0.07
L_{anom}	$\mathcal{U}(0, 0.5)$	0.19	0.29	0.43	0.49	0.5	0.06
c_w	$\mathcal{U}(0.5, 1.5)$	0.5	0.64	1.19	1.48	1.5	0.25
f_n	$\mathcal{U}(1, 10)$	1	1.37	3.85	8.87	10	2.25
u_n	$\mathcal{U}(100, 500)$	217.09	245.48	268.86	302.43	322.44	17.7
c_0	$\mathcal{U}(0, 1)$	0.03	0.15	0.32	0.64	0.77	0.15
c_1	$\mathcal{U}(0.1, 0.9)$	0.1	0.17	0.39	0.69	0.85	0.17
c_2	$\mathcal{U}(-15, 15)$	-9.65	-4.81	2.71	14.51	15	6.68
c_3	$\mathcal{U}(0.2, \pi/2)$	0.23	0.26	0.32	0.35	0.37	0.02
c_4 (10^x)	$\mathcal{U}(18, 22)$	18.52	19.23	20.15	20.33	20.44	0.34
c_5 (10^x)	$\mathcal{U}(14, 18)$	14	14.02	14.26	14.98	15.63	0.31

Variables with the (10^x) notation indicate a log-uniform distribution.

the posterior, and the median prediction moves closer to the experimental data.

The cathode coupling voltage is well-recovered under the posterior, including the non-monotonic trend with increasing background pressure. However, our predicted trend is more subtle than the experimental trend and peaks at a different pressure. This contrasts with our previous work, which was able to more tightly reduce the uncertainty in the cathode parameters and thus better capture the trend in the data. This is likely a result of

the likelihood used in this work, which prioritized *relative* error over the dataset rather than point-wise *absolute* error as in the previous work. We observed this outcome as well in the calibrated cathode parameters in Tab. IV, where overall relative error is greatly reduced by fine-tuning the V_{vac} parameter, but the (P_T, P^*, T_{ec}) parameters that characterize the more subtle trend with background pressure contribute less to the likelihood and so were calibrated to a much lesser extent. It is possible however, that given additional time, the calibration

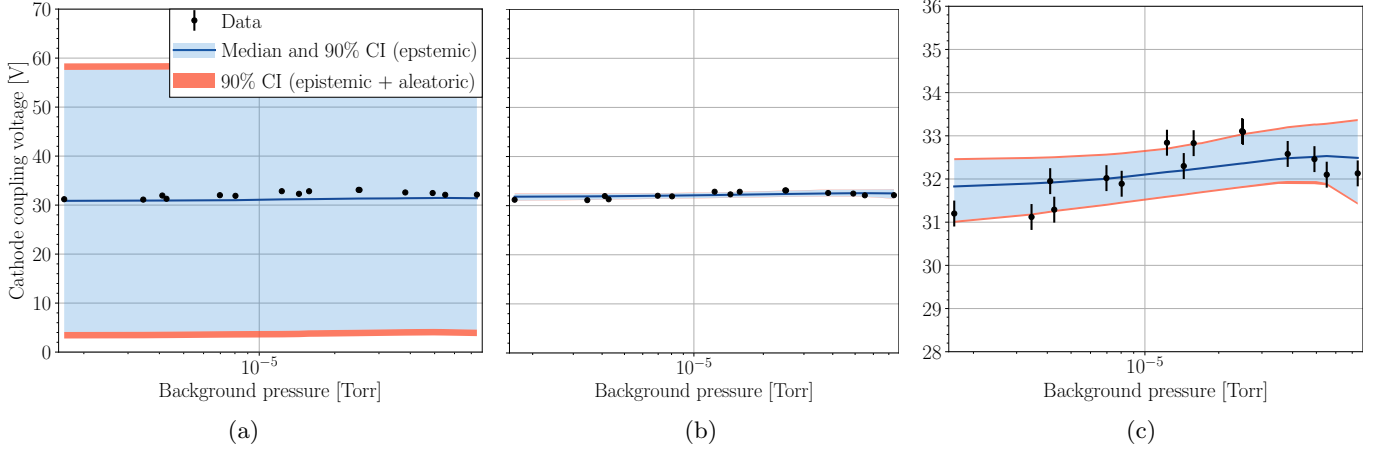


FIG. 4: (a) Prior, (b) posterior, and (c) zoomed-in posterior predictions of the SPT-100's cathode coupling voltage as a function of background pressure, compared to data from Ref. 21.

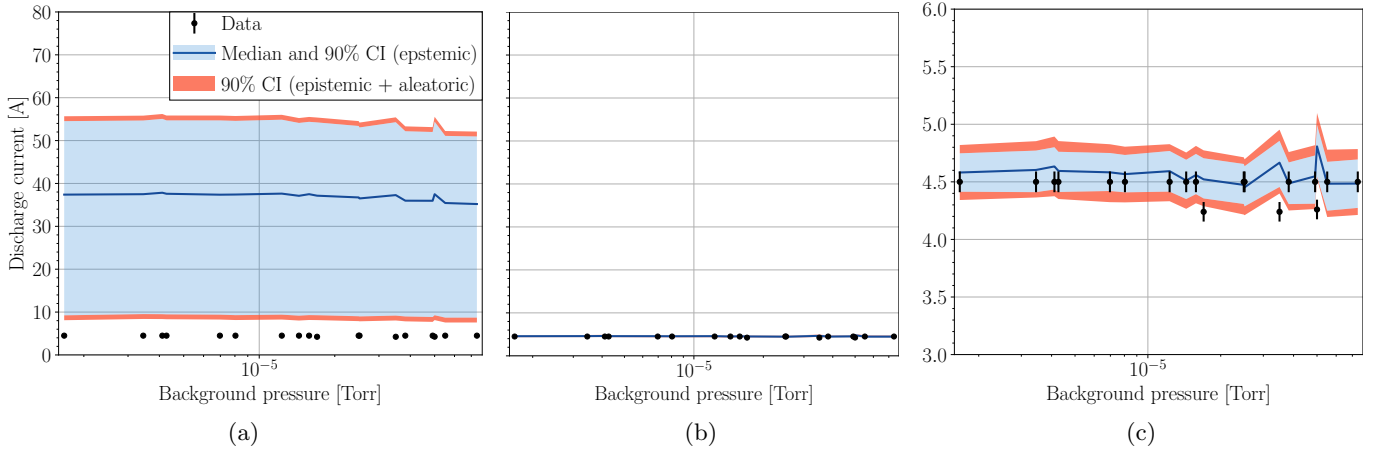


FIG. 5: (a) Prior, (b) posterior, and (c) zoomed in posterior predictions of the SPT-100's discharge current as a function of background pressure compared to data from Refs. 21 and 16.

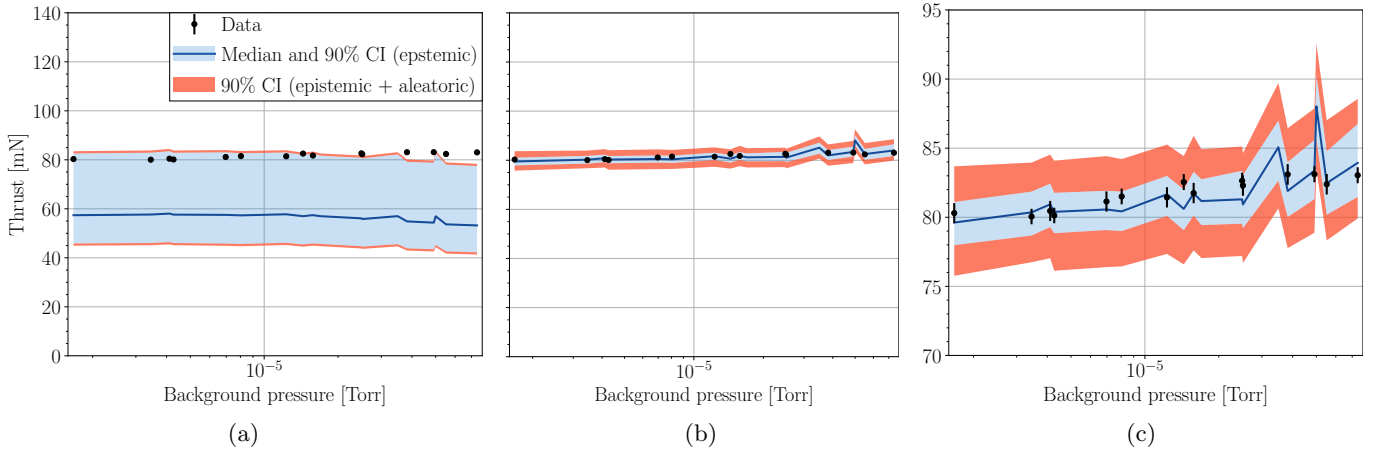


FIG. 6: (a) Prior, (b) posterior, and (c) zoomed-in posterior predictions of the SPT-100's thrust as a function of background pressure compared to data from Ref. 21.

procedure may have fine-tuned these parameters more to better fit the experimental trend.

The correct flat trend in discharge current with respect to background pressure is recovered in Fig. 5, though the 4.25 A points from Ref. 16 lie slightly outside of the CI. The experimental thrust is also encompassed within the posterior predictive CI bounds and exhibits the correct trend with pressure, i.e. slightly increasing with background pressure. For cathode coupling voltage and discharge current, the epistemic uncertainty is much larger than the aleatoric uncertainty, while for thrust the aleatoric uncertainty is equal to or greater than the epistemic uncertainty. This likely stems from the fact that thrust is directly impacted by thrust and flow rate, whereas discharge current and cathode coupling voltage are more indirectly-affected.

In Fig. 7, we compare the simulated ion velocity to measurements from Ref. 16. Our model captures the upstream shift in ion acceleration region with increasing background pressure as well as the maximum slope of the ion acceleration profile. In the data, the ion velocity profile at $P_B = 35 \mu\text{Torr}$ actually sits about 1 mm further upstream than that at $P_B = 50 \mu\text{Torr}$. The authors of the original paper noted that this was unexpected, as in most thrusters the acceleration region shifts monotonically upstream with pressure. As our model also assumes monotonicity, we do not capture this feature of the data. The main discrepancies with data occur upstream of the acceleration region, inside of the discharge channel ($z/L_{ch} < 1$), where the model overestimates the ion velocity. The reason for this overestimate is unclear, but likely has to do with the large ion backflow region (where $u_{ion} < 0$) seen in the data, which is unusual compared to ion velocity measurements on other thrusters. As an example of the level of model uncertainty typical for these predictions, we show in Fig. 7b the uncertainty bounds for the prediction at $35 \mu\text{Torr}$.

In Fig. 8, we show the plume ion current density profile at a distance of 1 meter from the thruster exit plane, compared to data from Ref. 21. For visual clarity, we only show three representative pressures out of the eight in the dataset. The model agrees with the data well, especially at angles less than 60 degrees. At larger angles, the absolute errors remain low while the relative error increases; this effect is magnified visually by the use of the logarithmic y-axis scale in Fig. 8. The likelihood used during calibration implicitly weights points with larger magnitudes higher than those with lower magnitudes. As very small current densities at large angles do not contribute much to the divergence angle integrals in Eq. 6, this choice prioritizes fitting the parts of the ion current density curve with a direct impact on thrust.

2. H9

We next examine the training performance for the H9 thruster. In Figs. 9, 10, and 11, we show the prior and

posterior predictions of the cathode coupling voltage, discharge current, and thrust from the H9.

The cathode coupling voltage is well-captured, with a clear monotonic trend with background pressure recovered by the model. The uncertainty in discharge current has been significantly reduced, and the model accurately predicts around the true value of 15 A. In contrast to the SPT-100 results, the model predicts a decreasing trend in thrust at high background pressures. We return shortly to a discussion of possible reasons for this puzzling trend.

In Fig. 12, we plot the H9's ion velocity predictions at three representative pressures. We observe both good agreement between the model and data as well as low prediction uncertainty. In particular, the final exit velocity, the pressure-dependent acceleration region shift, and the steepness of the acceleration profile are all captured faithfully. This agreement is enabled by the flexibility of the empirical anomalous transport model described in Sec. II A 2.

The current density dataset for the H9 includes measurements at multiple background pressures, each in turn taken at several distances from the thruster. For visual clarity, we first show results at a single distance and multiple pressures, followed by results at multiple distances and a single pressure. Fig. 13a, shows the ion current density curves at distance of 1.32 meters from the thruster and multiple pressures. As our chosen model form requires that the ion current density peak at zero degrees and decay monotonically with increasing angle, we are unable to capture the observed peak in the data at 7 degrees off-axis. However, we successfully reproduce both the peak current density and the trends with background pressure for angles up to 40 degrees. As in the SPT-100 data, this departure from the data at larger angles is reflected in Fig. 13b as increased uncertainty. Unlike in the SPT-100, the divergence angle of the H9 increases with pressure, which directly reduced the thrust at higher pressures. Without thrust data in the training dataset, this trend was unable to be counteracted by changes in other parameters during the calibration procedure. Finally, we plot in Fig. 14 the current density at all four radii in the training dataset, at a fixed pressure of $26.10 \mu\text{Torr}$. This demonstrates that our calibrated model accurately captures trends with distance as well as pressure.

3. Training performance

A more quantitative picture of the training performance can be obtained by examining the relative L_2 error of the calibrated model with respect to the training data. Given N samples of parameters θ and operating conditions \mathbf{d} from the prior or posterior distributions, we calculate the mean and standard deviation of the L_2 error in a QoI q

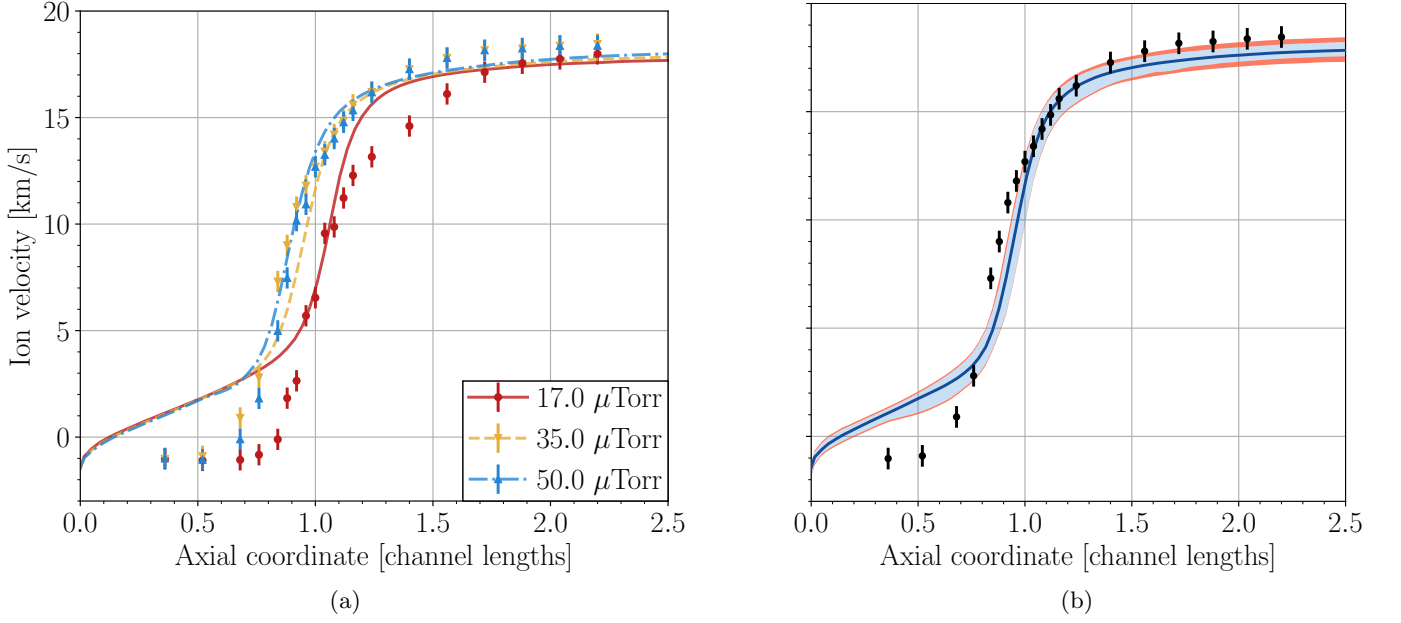


FIG. 7: (a) Median of posterior predictions of the SPT-100's axial ion velocity at three background pressures, compared to data from Ref. 16, (b) Median posterior prediction and uncertainty in ion velocity at $P_B = 35.0 \mu\text{Torr}$.

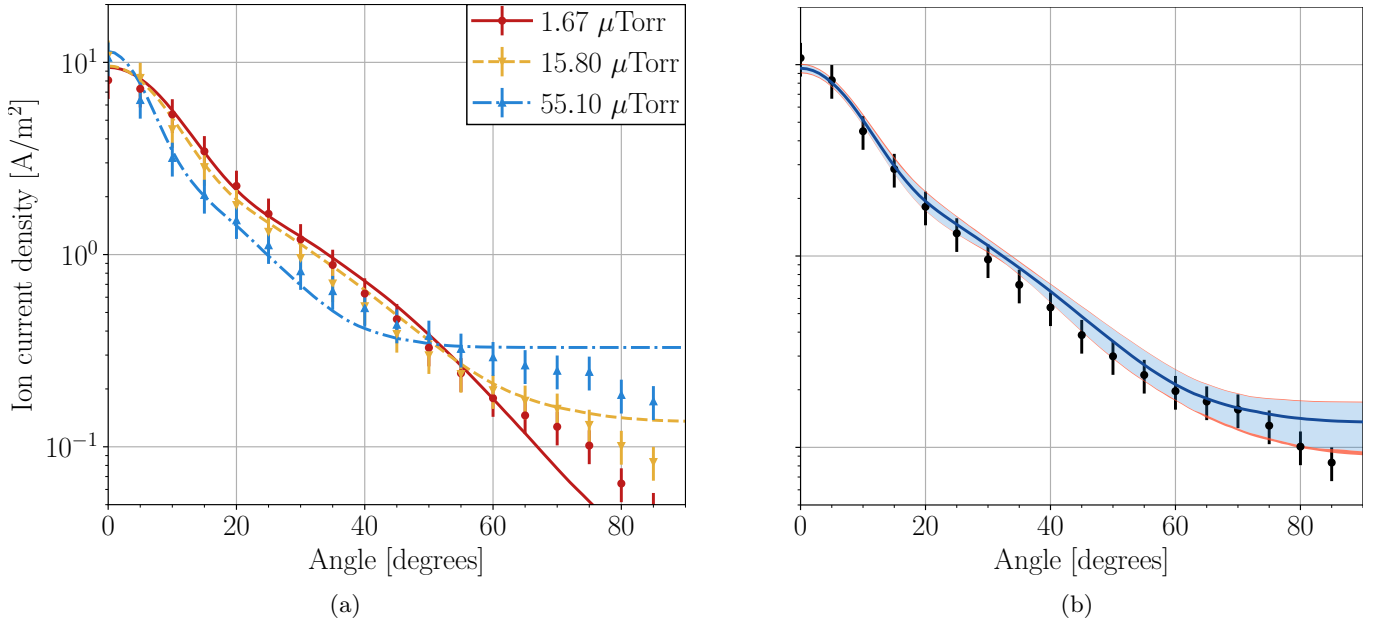


FIG. 8: (a) Median of posterior predictions of the SPT-100 plume ion current density distribution at $r = 1 \text{ m}$ compared to data from Ref.²¹. (b) Median posterior prediction and uncertainty in ion current density at $r = 1 \text{ m}$ for the $P_B = 15.80 \mu\text{Torr}$ condition.

as

$$E_q(\mathbf{x}) = \frac{\|\mathbf{y}_{eq} - f_q(\mathbf{x})\|}{\|\mathbf{y}_{eq}\|} \quad (9)$$

$$\mu_q = \frac{1}{N} \sum_{j=1}^N E_q(\mathbf{x}_j) \quad (10)$$

$$\sigma_q = \sqrt{\frac{1}{N} \sum_{j=1}^N [E_q(\mathbf{x}_j) - \mu_q]^2}, \quad (11)$$

where $E_q(\mathbf{x})$ is the relative L_2 error in QoI q between the model and data for input parameters \mathbf{x} . In Tabs. VI and VII, we report these errors for the SPT-100 and H9 respectively for $N = 1000$ samples of the inputs \mathbf{x}_j drawn from the prior and posterior input distributions as described in Sec. IID. For comparison, we additionally report the errors when the model is evaluated at the median parameter values ($\mu_{50} = E(\mathbf{x}_{50})$) as well as the ratio

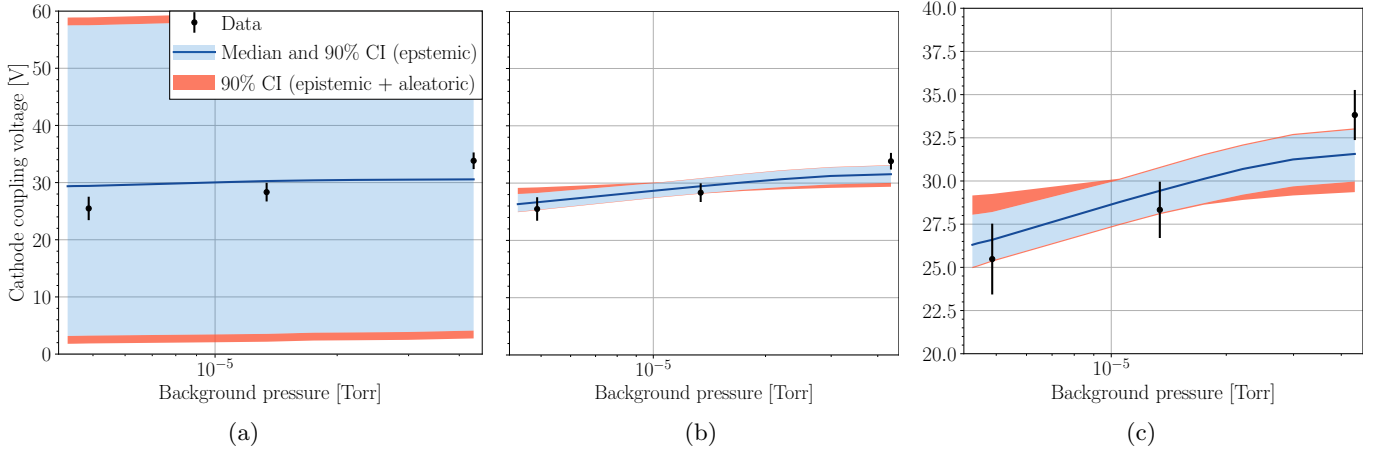


FIG. 9: (a) Prior, (b) posterior, and (c) zoomed-in posterior predictions of the H9's cathode coupling voltage as a function of background pressure compared to data from Ref 23.

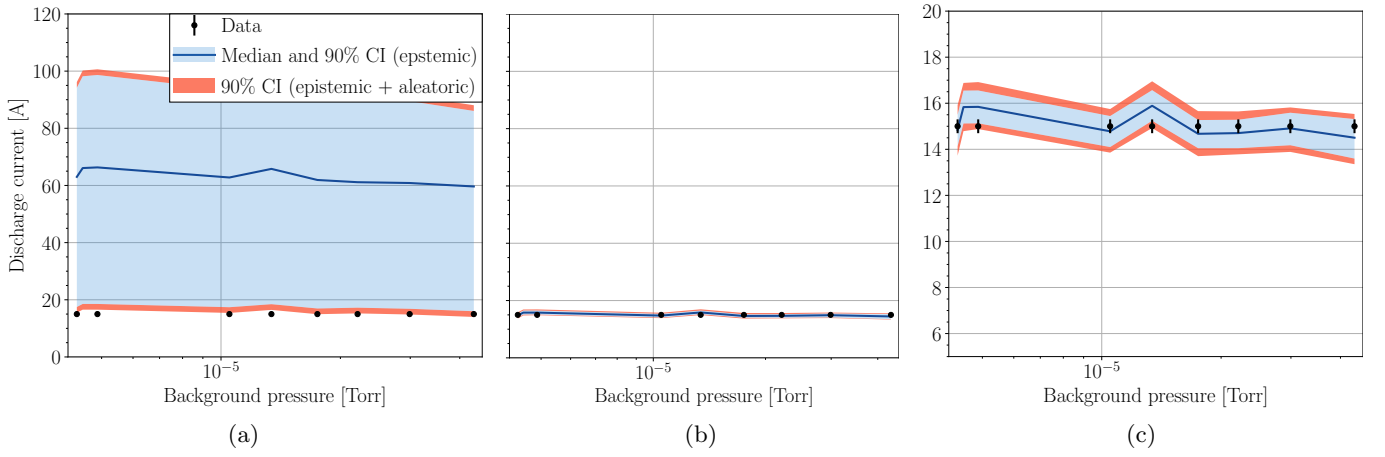


FIG. 10: (a) Prior, (b) posterior, and (c) zoomed-in posterior predictions of the H9's discharge current as a function of background pressure, compared to experimental data from Ref 23

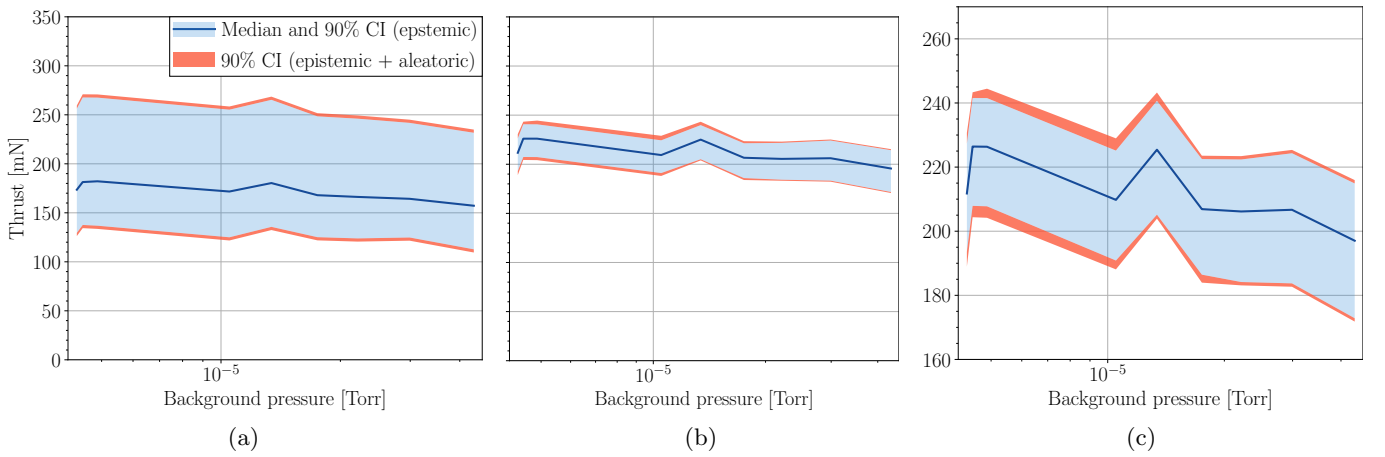


FIG. 11: (a) Prior, (b) posterior, and (c) zoomed-in posterior predictions of the H9's thrust as a function of background pressure.

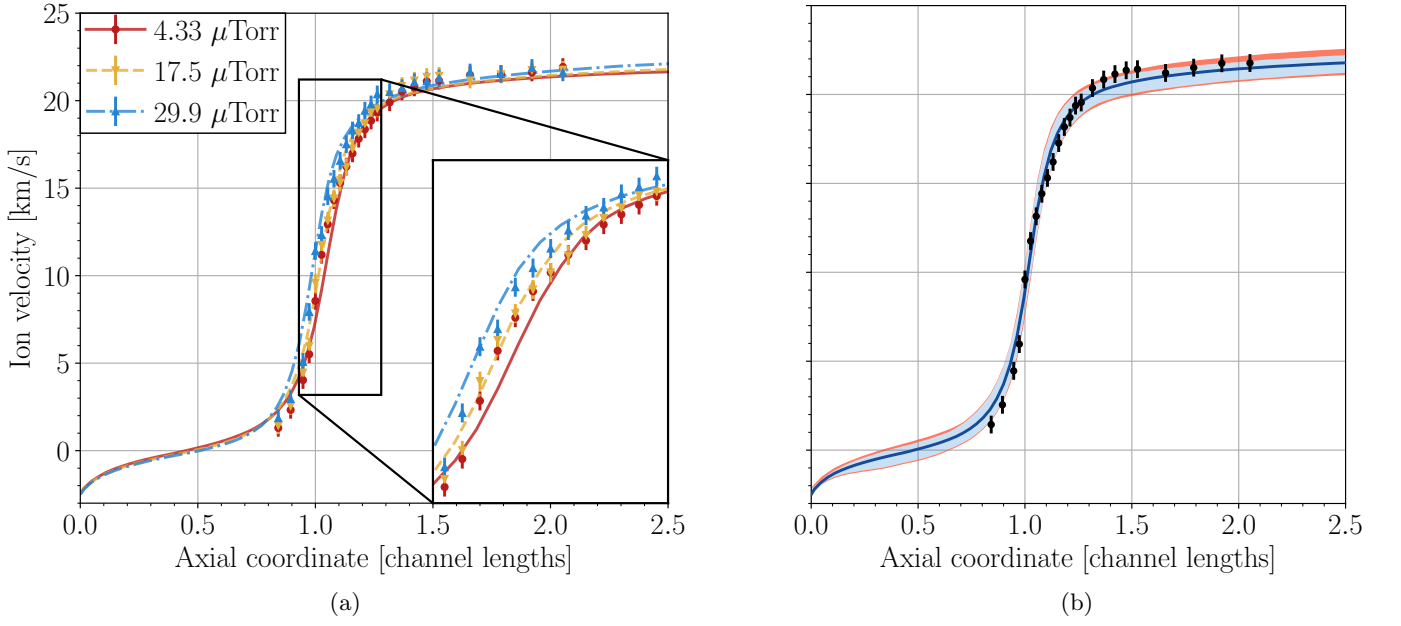


FIG. 12: (a) Median of posterior predictions of the H9's axial ion velocity at three background pressures, compared to data from Ref. 22 (b) Median posterior prediction and uncertainty in ion velocity at the $P_B = 17.5 \mu\text{Torr}$ condition.

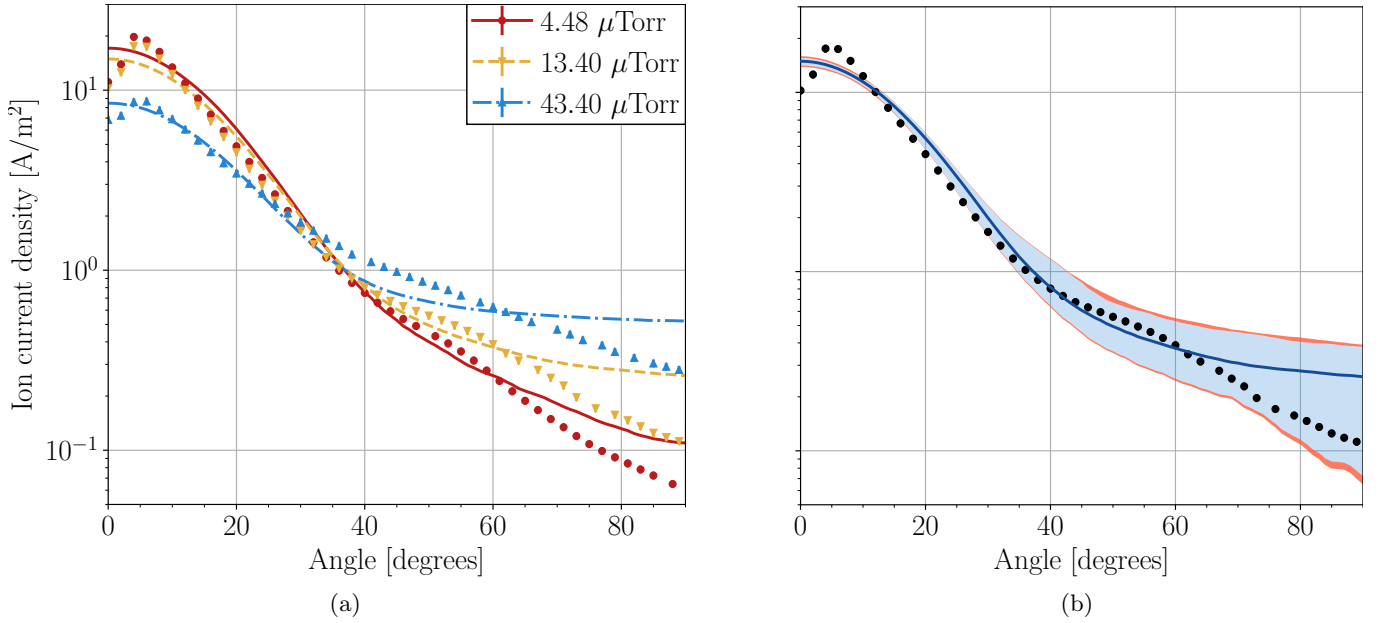


FIG. 13: (a) Median of posterior predictions of the H9 plume ion current density distribution at $r = 1.32 \text{ m}$. (b) Median posterior prediction and uncertainty in ion current density at $r = 1.32 \text{ m}$ and $P_B = 13.4 \mu\text{Torr}$.

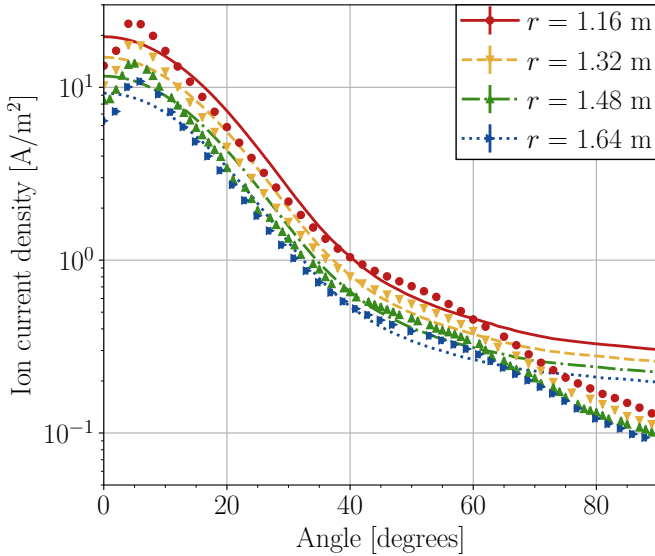


FIG. 14: Median of posterior predictions of the H9 plume ion current density distribution at multiple radii and $P_B = 13.4 \mu\text{Torr}$.

between the error and the nominal relative measurement uncertainties (ξ) used in our previous work.¹⁰ A value of $\mu_{50}/\xi \sim 1$ indicates that the model fits the data within the experimental uncertainty. We note that these metrics are identical to those in our previous work, which facilitates a direct comparison for determining improvement in the models; we include in Tab. VI the model and surrogate errors from the results of the previous work (note that a surrogate was not required in the present work due to optimizations in the thruster code).

All QoIs have a posterior μ_{50}/ξ of order 1 and show large improvement from the prior. For the SPT-100, most QoIs also show improvement over both the model and surrogate from previous work. The error in V_{cc} is higher than the previous model, which is likely explained by the wide posterior distributions of T_{ec} and P_T as discussed in Sec. III A. We note that the goal of the previous work was to calibrate the true model using the surrogate as a proxy, and we show in Tab. VI that the model in the present work shows considerably greater accuracy compared to the previous model for all QoIs (except V_{cc}). There are some cases, such as for thrust, where the surrogate from the previous work performs better than our model, but the ultimate goal is accuracy in the true model, for which the present work demonstrates better performance (e.g. by a factor of eight for thrust). In all cases, the standard deviation of the errors, σ , is higher than our previous work. While this may seem at first like a negative result, it in fact demonstrates the success of our new likelihood function. In that work, the uncertainty in our predictions was very low, and in many cases the data lay well outside of the uncertainty bounds. Our updated procedure allows for larger predictive uncertainty which more accurately captures the state of our knowledge post-calibration.

The H9 model (Tab. VII) fits the data well for all quantities, although here the interpretation of μ_{50}/ξ is more complicated. For comparing to the SPT-100 data, we use the same nominal measurement uncertainty values, though we note that the uncertainty in the cathode coupling voltage for the H9 was closer to 2.5%. This would bring μ_{50}/ξ down to 2.24, which is consistent with the error for the SPT-100 cathode coupling voltage.

B. Test performance

In this section, we assess the ability of the calibrated model to extrapolate to operating conditions outside of the training dataset. To this end, we use the test datasets described in Sec. II B. In Fig. 15, we plot the prior and posterior predictions of discharge current (Fig. 15a) and thrust (Fig. 15b) for the SPT-100 dataset from Ref. 17. We show in Fig. 16 the same QoIs for the H9 dataset in Ref. 24. These plots compare the predicted QoI to the experimental value, with good agreement indicated by points lying close to the dashed black $y = x$ line. We also report in Tab. VIII the same L_2 error metrics as in Sec. III A 3.

The SPT-100 model predicts the test data well and outperforms the model from previous work, though with errors larger than those seen for the training data. The standard deviation in thrust and discharge current errors is reduced to below 2.5%, and the posterior median errors are below 10%. Additionally, the model tends to slightly under-predict the experimental thrust. The model predicts the correct discharge current for the H9 with an error of just 1.3%, with a standard deviation of 1.8%; this good agreement is unsurprising in light of the fact that the discharge current was a constant 15 A in both training and test datasets. Despite lacking thrust in the training data, the H9 model is able to improve on the prior predictions for thrust and obtain a median prediction error of 10%. The error standard deviation has additionally been reduced by a factor of four from the prior, but the predicted thrusts underestimate the experimental values in all cases.

Taken together, these results show that the calibrated models of both the H9 and SPT-100 are able to extrapolate beyond their training datasets. This was especially observed for the SPT-100, and it is likely that the performance of the H9 model would improve if a wider range of training conditions is made available (i.e. more discharge currents and thrust data).

C. Extrapolation to orbit

We now turn to using the calibrated model to attempt extrapolation of SPT-100 ground test data to space. We report in Tab. IX predictions of the SPT-100 thrust and discharge current for the on-orbit Express satellite test dataset.³

TABLE VI: Relative L_2 error between model predictions and training data for the SPT-100. ξ is the nominal experimental error in the data, μ is the mean error, σ is the standard deviation of the error, and μ_{50} is the prediction error at median parameter values. This work is compared to surrogate and model results from previous work.¹⁰

SPT-100			L_2 error [%]			
QoI	ξ [%]	Distribution	μ_{50}	μ	σ	μ_{50}/ξ
V_{cc} [V]	1	Prior (this work)	4	45.9	26.8	4
		Posterior (this work)	2.5	2.8	0.5	2.5
		Posterior (prev. work, model)	2	-	-	2
T_c [mN]	1	Prior (this work)	30.4	27.6	13.3	30.4
		Posterior (this work)	3.3	3.5	0.5	3.3
		Posterior (prev. work, model)	29	-	-	29
		Posterior (prev. work, surrogate)	2.5	2.6	0.2	2.5
I_D [A]	10	Prior (this work)	728.9	667.9	324.3	72.9
		Posterior (this work)	3.3	3.9	1.4	0.3
		Posterior (prev. work, model)	63	-	-	6.3
		Posterior (prev. work, surrogate)	45	45	0.3	4.5
u_{ion} [m/s]	5	Prior (this work)	24.2	25	4.8	4.8
		Posterior (this work)	12.2	13.8	1.3	2.4
		Posterior (prev. work, model)	17	-	-	3.4
		Posterior (prev. work, surrogate)	21	21	0.2	4.2
j_{ion} [A/m ²]	20	Prior (this work)	87.2	80.7	15.4	4.4
		Posterior (this work)	11.4	18.6	1	0.6
		Posterior (prev. work, model)	49	-	-	2.4
		Posterior (prev. work, surrogate)	33	33	0.3	1.6

TABLE VII: Relative L_2 error between model predictions and training data for the H9. Symbols have the same meanings as Tab. VI.

H9			L_2 error [%]			
QoI	ξ [%]	Distribution	μ_{50}	μ	σ	μ_{50}/ξ
V_{cc} [V]	1	Prior	10.7	53.8	28.4	10.7
		Posterior	5.4	6.1	1.3	5.4
I_D [A]	10	Prior	318.2	301.9	157	31.8
		Posterior	3.4	4.3	1.1	0.3
u_{ion} [m/s]	5	Prior	45.8	43.6	8.1	9.2
		Posterior	4.1	5.3	1	0.8
j_{ion} [A/m ²]	20	Prior	82.6	76.9	18.6	4.1
		Posterior	18.9	19.5	0.5	0.9

The discharge current is captured to within 5% of the experimental value in both cases, and we correctly predict that the current should increase slightly between the ground and orbit. We also recover the thrust to within 10%, though as in the test dataset from Ref. 17 we under-predict the thrust in both cases. Unfortunately, we predict that the thruster should exhibit higher thrust on orbit than on the ground, which conflicts with the trend in the data. As shown in Fig. 6, the model was able to predict the correct trends in thrust with back-

ground pressure in the training dataset. However, those simulations each were performed at a discharge voltage of 300 V, while the SPT-100 from Ref. 3 operated at 310 V on orbit. During training, the model was thus unable to learn anything about how performance and plasma properties should scale with changes in discharge voltage. The effects of the voltage discrepancy between on-ground and on-orbit operation in this case likely overwhelmed the pressure-dependent effects, causing the model to predict the wrong trend. Additionally, the mass flow rate was

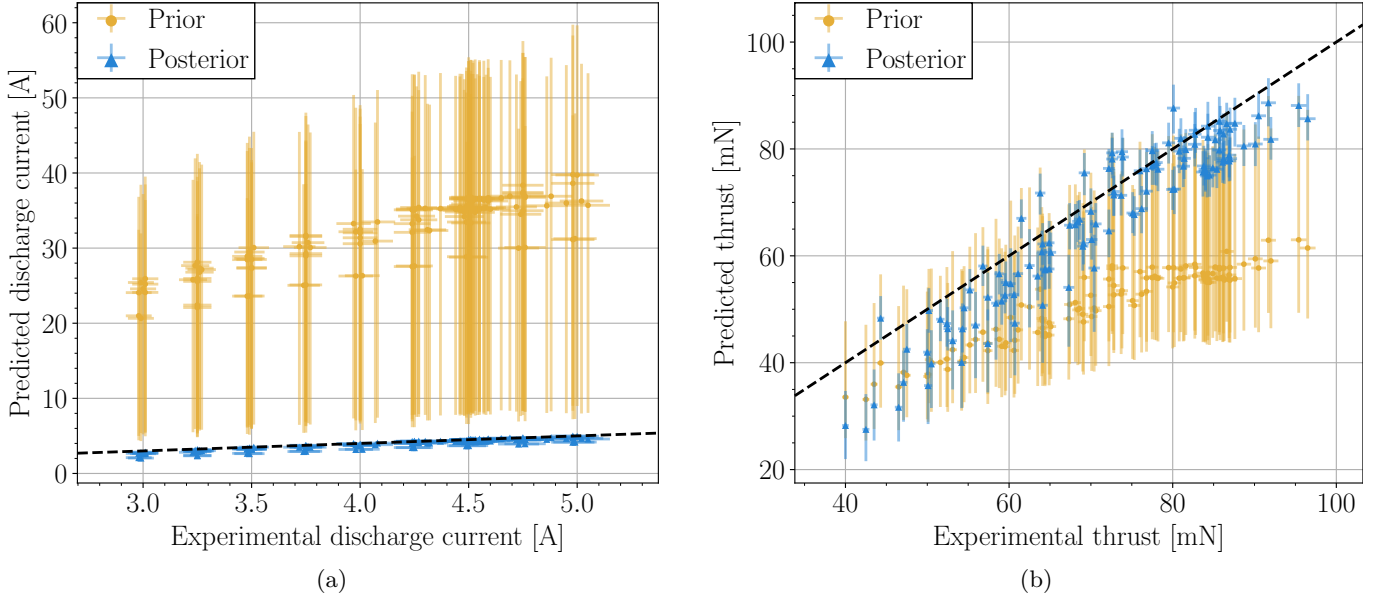


FIG. 15: Prior and posterior predictions of (a) discharge current and (b) thrust for the SPT-100 Hall thruster from the test dataset in Ref. 17. Perfect agreement ($y = x$) is indicated by the dashed black line. Horizontal error bars indicate the experimental error while vertical bars represent the range between the 5th and 95th percentiles of predictions. The median prediction is indicated by a marker.

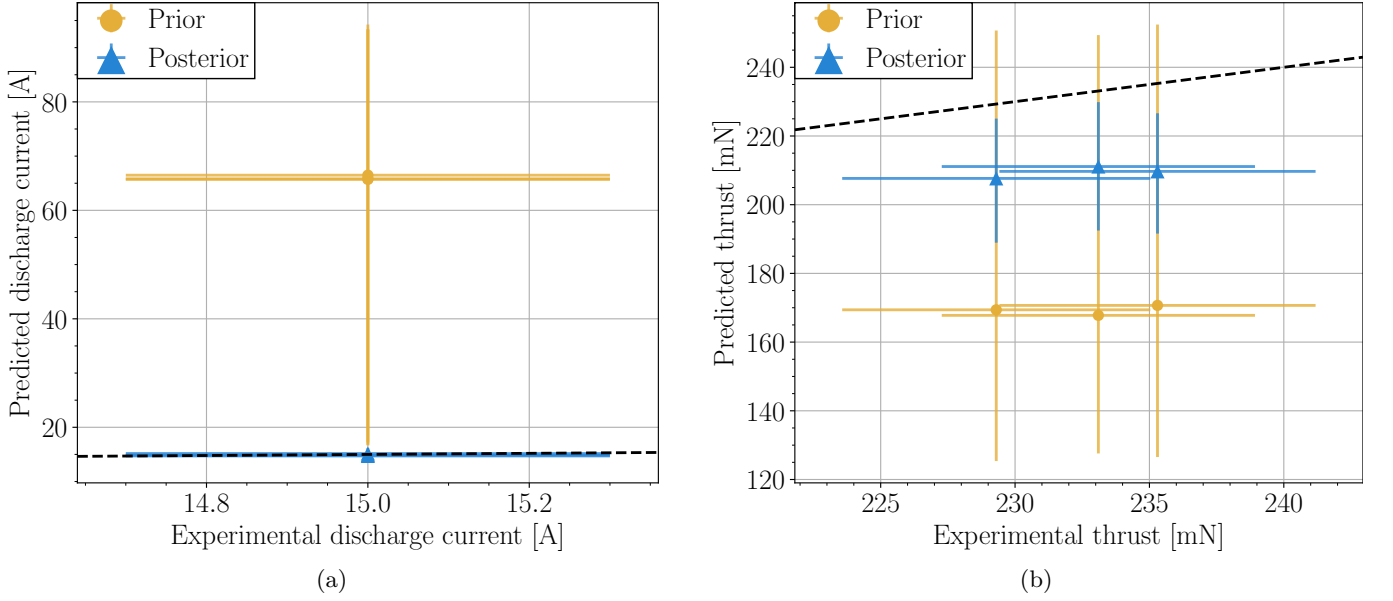


FIG. 16: Prior and posterior predictions of (a) discharge current and (b) thrust for the H9 Hall thruster from the test dataset in Ref. 24). Plot features have the same meanings as in Fig. 15.

not measured for either on-ground or on-orbit operation in this dataset, making it challenging to reproduce the operating conditions accurately.

D. Anomalous electron transport

The magnitude and scaling of the anomalous electron transport are known to have a large impact on Hall thruster model results compared to other parameters. Indeed, in our prior work,¹⁰ we found that at least 60% of the variance in the ion velocity predictions and 20% of the variance in thrust could be explained by uncertainty

TABLE VIII: Relative L_2 error between model predictions and test data for the SPT-100 and H9. The SPT-100 test data comes from Ref. 17 and the H9 test data from Ref. 24. Previous work values come from Ref.¹⁰. Symbols have the same meanings as Tab. VI.

SPT-100			L_2 error [%]			
QoI	ξ [%]	Distribution	μ_{50}	μ	σ	μ_{50}/ξ
T_c [mN]	1	Prior (this work)	29.8	28.3	12	29.8
		Posterior (this work)	9.6	10.4	1.8	9.6
		Posterior (prev. work, model)	30	-	-	30
		Posterior (prev. work, surrogate)	7	7	0.1	7
I_D [A]	10	Prior (this work)	672.9	622.2	325.1	67.3
		Posterior (this work)	8.9	9.6	2.4	0.9
		Posterior (prev. work, model)	53	-	-	5.3
		Posterior (prev. work, surrogate)	40	40	0.1	4
H9			L_2 error [%]			
QoI	ξ [%]	Distribution	μ_{50}	μ	σ	μ_{50}/ξ
T_c [mN]	1	Prior	27.2	25.6	14.8	27.2
		Posterior	10	10.4	3.8	10
I_D [A]	10	Prior	340	315.1	156.3	34
		Posterior	1.3	3.8	1.8	0.1
j_{ion} [A/m ²]	20	Prior	88.6	81.3	17.3	4.4
		Posterior	34.3	34.4	1.8	1.7

TABLE IX: SPT-100 thrust and discharge current from the Express-A satellites³ compared to model.

QoI	Case	Data	Sim. median	Sim. 5th pctl	Sim. 95th pctl
Thrust [mN]	Ground	84.6 ± 2.4	75.2	71.2	78.7
	Orbit	83.3 ± 3.2	76.6	73.1	80.3
Discharge current [A]	Ground	4.5	4.3	4.06	4.53
	Orbit	4.6 ± 0.1	4.33	4.1	4.58

in the anomalous transport parameters. Here, we briefly analyze the calibrated anomalous electron collision frequency profiles and the uncertainty in the five transport parameters.

In Fig. 17, we show the profiles of the anomalous electron collision frequencies for the SPT-100 and H9 at three pressures each. As designed, the profile moves upstream at higher pressures. The uncertainty in the axial position of the profile is very low, as reflected by the distributions of parameters z_{anom} and L_{anom} in Tabs. IV and V. The uncertainty in the magnitude of the anomalous transport at the bottom of the Gaussian trough is similarly low. The posterior for the parameter that governs this, β_{anom} , lies in the range (0.95, 1) for both thrusters, from a prior range of (0, 1). In contrast, the maximum magnitude of the anomalous transport (governed by α_{anom}) has high uncertainty, spanning at least a factor of two for both thrusters. This result is in line with similar observations by Mikellides and Lopez-Ortega,^{7,26} as well as those by Hara and Mikellides,²⁷ which found that the near-anode anomalous collision frequency mainly affects thrust and

ionization oscillations, with less effect on the ion velocity profile. This also explains the larger uncertainty in α_{anom} for the H9, as without thrust data the near-anode electron transport was not as constrained as for the SPT-100.

IV. DISCUSSION

In this work, we applied Bayesian inference to calibrate a coupled multi-component Hall thruster model against experimental data for the SPT-100 and H9 thrusters. We used these models to produce probabilistic predictions of several quantities of interest (QoIs), including thrust and spatially-resolved ion velocity, at different operating conditions and background pressures. Across most QoIs, the models of both thrusters exhibited training and test errors of less than 10%, with the SPT-100 model outperforming previous work. We now turn to a discussion of the results, beginning a summary of our core findings. We then discuss some of the challenges we encountered and the primary sources of uncertainty in our predictions.

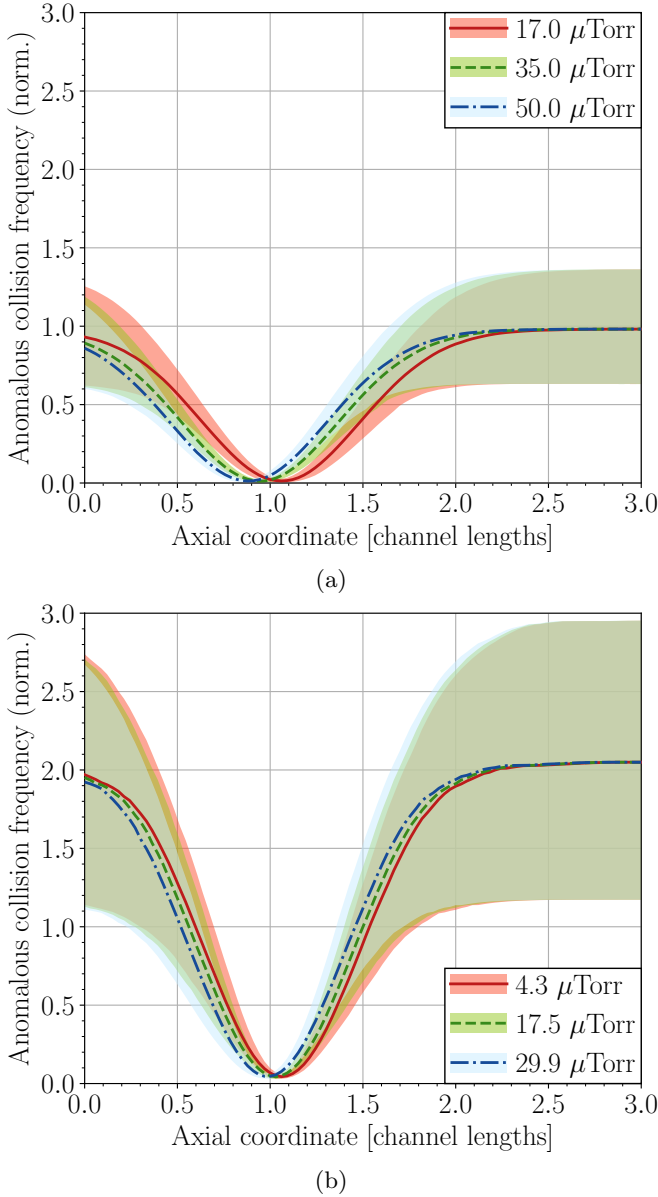


FIG. 17: Posterior estimates of the anomalous electron collision frequency for the (a) SPT-100 and (b) H9, at three background pressures each. The collision frequencies are normalized by the Bohm diffusion value of $\nu_{bohm} = \omega_{ce}/16$.

Finally, we outline some ways in which the results might be improved.

A. Core findings

1. Bayesian inference is an effective tool for calibrating and quantifying uncertainty in Hall thruster models. Our calibration procedure automatically and robustly explored and optimized over a large and high-dimensional parameter space. For all QoIs,

it reduced uncertainty in predictions and improved the model's accuracy over the prior without manual intervention. Additionally, we optimized over the entire dataset at once, in parallel, instead of tuning the model parameters per-condition. These results demonstrate the usefulness of Bayesian methods for calibration in the context of predictive Hall thruster modeling.

2. The calibrated models fit the training data well and can generalize to unseen test data. The models and parameterizations we used in our coupled framework captured the correct trends in the training data across many background pressures. In addition to high training accuracy across most QoIs, we also observed $\leq 10\%$ median test error on thrust and discharge current for both the SPT-100 and H9 thrusters. When extrapolating SPT-100 data to orbit, the models predicted the wrong trend in thrust, but correctly captured the trend in discharge current, with median errors $\leq 10\%$ for both quantities. Additionally, modeling changes in this work related to facility effects and anomalous transport were the primary cause of increased performance over our previous work¹⁰ (see Appendix B).

3. The phenomenological anomalous transport models were successful at predicting ion velocity profiles at varying pressures. In this work, we introduced a new four-parameter empirical model for the anomalous electron transport and a simplified logistic pressure-dependent model for the location of the acceleration region. Together, these models were able to reproduce the experimentally-observed trends in ion velocity with high accuracy. In particular, the median ion velocity error for the H9 was less than 5%. Lastly, we note that neglecting the upstream pressure shift, the posterior anomalous transport parameters were very similar between the H9 and SPT-100. We believe that the four-parameter model with $\alpha_{anom} = 1/16$, $\beta_{anom} \approx 0.99$, $z_{anom} \approx 1.05$, and $L_{anom} \approx 0.38$ may be a good default choice when simulating other thrusters at 300 V, though it remains necessary to verify this with other codes. However, we note that these parameters may not generalize well to thrusters operating at higher voltages.

B. Sources of uncertainty

In Sec. II, we described the difference between aleatoric and epistemic uncertainty. The results showed that aleatoric uncertainty was a minor component of overall uncertainty, with epistemic uncertainty due to the posterior distributions of model parameters making up the largest part. In addition, there remains uncertainty due to the choice of models and parameters and due to the data.

1. Model uncertainty: This uncertainty was most evident in predictions of ion velocity for the SPT-100 and ion current density for the H9. In both cases, the

epistemic and aleatoric uncertainties were low while large discrepancies from the experimental data remained. This mismatch reflects the inability of the chosen model form to accurately capture features of the data, such as the off-axis peaks in the current density of the H9 or the extended ion backflow region of the SPT-100. The neutral ingestion model was another source of model uncertainty, as it was only partially successful at capturing trends in thrust with background pressure. For many QoIs, however, the model was capable of capturing the data within epistemic and aleatoric uncertainty.

2. Data uncertainty: The H9 training dataset did not contain thrust, which led the model’s thrust estimates to be poorly-constrained for this thruster. Additional uncertainty in model predictions may stem from the range of operating conditions available in the training data. At each training point, the discharge voltage was fixed at 300 V for both thrusters, and the discharge current was between 4.25 and 4.5 A for the SPT-100 and exactly 15 A for the H9. For both thrusters, the calibration procedure was unable to explore how the model responds to larger trends in mass flow rate or discharge voltage. Including a wider range of conditions in the training data may have reduced posterior uncertainty further and allowed the models to better generalize to the test data.

C. Future improvements

1. Upgrades to existing models: Much of the improvement from our previous work was enabled by iterative improvements to the thruster component model. This is likely to be true for future versions of the framework. A more complex anomalous transport model may be able to capture even more features of the ion velocity data, and an improved neutral ingestion model will certainly be required. Additionally, charge exchange collisions are not currently modeled by `HallThruster.jl` but are suspected to play a large role in some of the pressure-dependent phenomena observed experimentally.²⁸ Our analytic plume model currently cannot model distributions in which the peak current density occurs away from the thruster centerline. The flexibility of this model should be improved to be able to capture such trends. Improvements to the cathode coupling model are also possible—in particular, to be able to capture some of the differences between centrally- and externally-mounted cathodes.

2. New QoIs: In both this work and our previous work, we compared our simulation results to the same five QoIs—cathode coupling voltage, thrust, discharge current, ion velocity, and ion current density. Additional data sources are available that would further help refine our parameter estimates and motive modeling improvements. For instance, ion energy distribution function measurements made via retarding potential analyzer and species fraction measurements obtained from $E \times B$ probes both provide valuable physical insight into the state and evolution of

the Hall thruster plasma. Furthermore, time-resolved data remains an important and underutilized resource, and future versions of our model may be strengthened by attempting to match these data. Lastly, non-invasive laser measurements of the electron energy distribution functions^{22,29} are an increasingly important source of information about electron transport and plasma heating. In each case, updating our framework to be able to take advantage of these data will require changes to be made to both the component models and the calibration procedure.

3. New models: In addition to upgrading existing models, explaining some sources of data will require the addition of new models. Carbon back-sputter³⁰ and electrical and circuit effects⁵ stand out as two pressing facility effects which our framework does not attempt to model. Improving predictions of trends in thrust with background pressure may be possible by factoring out the neutral ingestion component of the thruster code into a dedicated sub-model. This model could be analytic, such as that of Frieman et al.,¹⁸ or take the form of a combined model for the plume and vacuum chamber³¹. Incorporating these more complex models requires a much larger amount of information about the thruster and test environment than we currently use, including detailed 2-D thruster geometric and magnetic field information, the distribution of cryopumps and ion gauges throughout the chamber, and the geometry of the facility and beam dump. This information is not readily available in the literature, so data availability may be low for calibrating these higher fidelity models.

To meet these challenges, we have improved the modeling framework to increase its modularity and flexibility by allowing component models to be quickly added or upgraded, and their parameters and couplings to be readily fine-tuned or adjusted. The framework allows us to rapidly test new models and parameter configurations and determine performance on different thrusters and facility effects. Already, we have demonstrated this modular approach by upgrading our original models¹⁰ and expanding the UQ calibration and analysis to new thrusters. We hope this framework will continue to expand as we improve the models and account for new facility effects.

4. Handling uncertain operating conditions: In many cases, especially when using data from the literature, we may not have full information about the operating conditions at which the data was obtained. This was evident in our attempts to predict the on-orbit performance of the SPT-100, in which we had to rely on “best guess” mass flow rates which may not have reflected reality. To handle these situations, we would need to take the uncertainty in these parameters into account during calibration and/or prediction more rigorously.

During calibration this would require marginalizing the aleatoric parameters out of the likelihood (we currently assume they are fixed at baseline values). During prediction, we would have to sample over a range of operating

conditions or provide worst case probabilistic predictions. Both of these approaches require significantly more computation, and are reserved for future work.

V. CONCLUSION

In this work, we developed an improved framework for rapid prediction of Hall thruster performance. By coupling cathode, thruster, and plume models with Bayesian inference, we can calibrate model parameters to data and predict important quantities with detailed uncertainty quantification. We used this model to reduce the uncertainty in many key parameters and obtained improved training performance over our previous work. We then demonstrated good generalization outside of the models’ training dataset and attempted to extrapolate the performance of a thruster operating on the ground to orbit. Furthermore we extended the model to simulate a magnetically-shielded thruster in addition to the SPT-100. These improvements were made possible due to modeling improvements, including a new empirical anomalous transport model, as well as changes to our Bayesian likelihood.

While these changes were largely successful, our work had some shortcomings. For instance, our calibration procedure was unable to find model parameters which captured trends in cathode coupling voltage with background pressure. Additionally, the lack of thrust data for the H9 led to poorly-calibrated predictions of this key QoI. Lastly, the model was trained over a limited range of operating conditions, limiting somewhat its extensibility across discharge voltages and larger changes in mass flow rate.

The current model serves both as a good standalone Hall thruster model as well as a useful baseline for future extensions. By incorporating new and upgraded models as well as additional data sources, we plan to continue improving the framework’s predictive power and generality.

ACKNOWLEDGMENTS

Funding for this work was provided by NASA in part through the Joint Advanced Propulsion Institute (JANUS), a NASA Space Technology Research Institute, under grant number 80NSSC21K1118, as well as in part through a NASA Space Technology Graduate Research Opportunity grant 80NSSC23K1181. This research was additionally supported in part through computational resources provided by Advanced Research Computing at the University of Michigan.

DATA AVAILABILITY

The code used for this study is open-source and available at <https://github.com/JANUS-Institute/HallThrusterPEM.git>. It builds on the open-source *AMISC* multidisciplinary modeling framework, available online at <https://github.com/eckelsjd/amisc.git>. The Hall thruster component of the model, *HallThruster.jl*, is on GitHub at <https://github.com/UM-PEPL/HallThruster.jl.git>. The datasets generated and analyzed during this study are available from the corresponding author on reasonable request.

Appendix A: Selected data from the Express satellites

Here, we summarize the data from the Russian Express satellites used in predicting the on-orbit performance of the SPT-100. This data was originally reported by Manzella et al. in 2001.³ Following the analysis of Byrne and Jorns,³² we use measurements only from thrusters that had been fired for over 30 hours in space, which was 50% longer than the manufacturer’s recommended burn-in time. The thrusters meeting this criteria were thrusters RT2 from Express-A #2 and RT1, T4, and RT4 from Express-A #3. We report in Tab. A.1 thrust measurements averaged across these thrusters. Note that the discharge current and voltage observed on-orbit were somewhat higher than the nominal values from the ground tests.

Appendix B: Intermediate model results

In this appendix, we show selected results for the SPT-100 Hall thruster using an “intermediate model” between the one in our previous paper¹⁰ and the one presented in this work. Here, we employ the inference and calibration procedure developed in Sec. II C but use a model parameterization similar to our previous work. Specifically, we use a two-zone Bohm-like anomalous transport profile, a four-parameter pressure shift model, and no wall loss or neutral ingestion parameters. This exercise allows us to assess how much of the improvement over our previous work stems from better sampling versus improved modeling.

First, in Fig. B.1 we show the discharge current and thrust predicted by the model after calibration. In contrast to the model of the present work, the discharge current of the previous model lies above the experimental value for all pressures and has an exaggerated pressure dependence. The thrust also exhibits overly-strong pressure-related trends. In Fig. B.2, we show the predicted ion velocity profiles of the previous model as a function of background pressure. The old pressure shift model captures the upstream displacement of the acceleration region well but is over-parameterized, requiring four parameters instead of just one as in the present work. Additionally,

TABLE A.1: Operational and performance data obtained on the ground and in orbit from two Express-A satellites. Data aggregated from Ref. 3. Mass flow rates (*) were not directly measured and are instead calculated in Ref. 3 by assuming a total xenon flow rate of 5.3 mg/s and a 7% cathode flow fraction.

Pressure [Torr]	\dot{m}_a [mg/s]	V_D [V]	I_D [A]	T [mN]	Note
2×10^{-6}	4.29*	300	4.5	84.6 ± 2.4	Ground tests
2×10^{-8}	4.29*	310	4.6 ± 0.1	83.3 ± 3.2	On-orbit measurements

Reported uncertainties are ± 2 standard deviations.

the new anomalous transport model better captures the shape and steepness of the ion velocity profiles. Finally, in Tab. B.1, we compare the training error metrics of the previous model to those of the present model. We find that the present model exhibits lower mean and median errors in thrust and discharge current by a factor of 60–90%. In all, these findings are approximately as good as those obtained in our previous work, although predict more exaggerated trends in discharge current and thrust with pressure than are observed in the data.

Appendix C: Posterior parameter distributions

In this appendix, we include plots of the 1-D and 2-D marginal posterior distributions for each model parameter obtained with Bayesian inference. Due to the large number of variables, we have broken these figures up by component for clarity. The cathode parameter marginals for the SPT-100 and H9 are in Figs. C.1 and C.4. We plot the thruster parameter marginals in Figs. C.2 and C.5, and the plume parameter marginals in Figs. C.3 and C.6.

We make a few observations beyond those made in Sec. III A. For both thrusters, the transport barrier length L_{anom} clusters at the upper end of its range, indicating that higher values may have given better results. Additionally, the anomalous pressure shift parameter Δz_{anom} correlates with z_{anom} , since both parameters shift axially the anomalous electron collision frequency. Across all components, we observe largely unimodal parameter distributions with the exception of c_2 for the H9 plume, which has two peaks. This parameter controls the pressure dependence on the divergence angle. Examining Fig. C.6, it is not immediately clear why this should be as we fit the trends with pressure well.

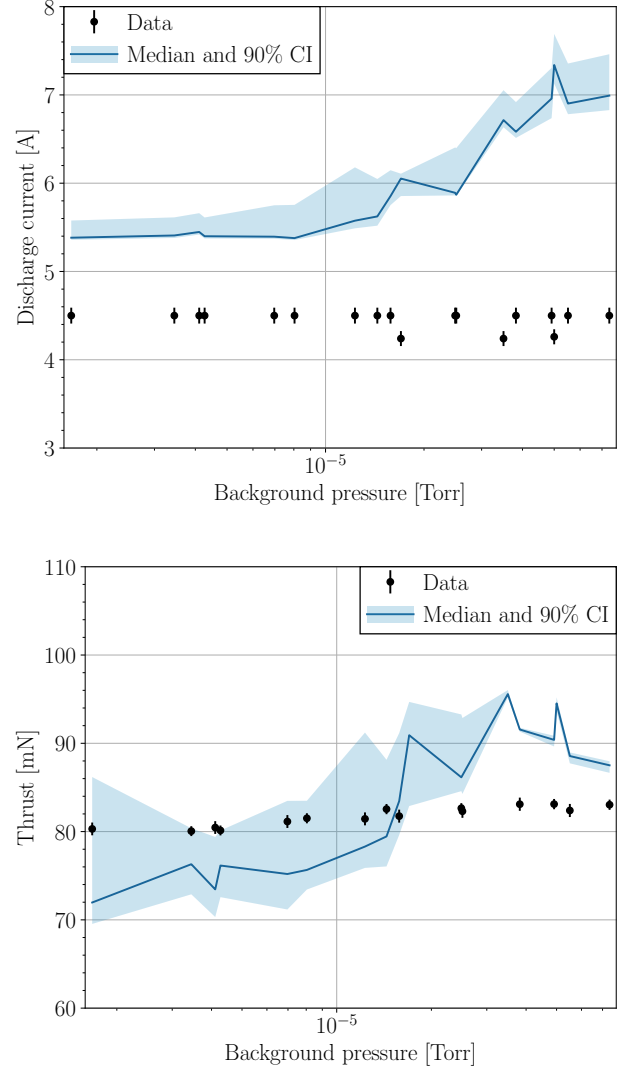


FIG. B.1: (a) Discharge current and (b) thrust vs pressure for the SPT-100 using the model of Ref. 10.

¹J.-P. Boeuf, “Tutorial: Physics and modeling of Hall thrusters,” *Journal of Applied Physics* **121**, 011101 (2017).

²T. Randolph, V. Kim, H. Kaufman, K. Kozubsky, V. Zhurin, and M. Day, “Facility Effects on Stationary Plasma Thruster Testing,” in *Proc. of the 23rd International Electric Propulsion Conference* (1993).

³D. Manzella, R. Jankovsky, F. Elliot, I. Mikellides, G. Jongeward, and D. Allen, “Hall thruster plume measurements on-board the Russian Express satellites,” in *27th International Electric Propulsion Conference, Pasadena, California* (2001) NASA/TM-2001-211217.

⁴W. Huang, H. Kamhawi, T. Haag, A. L. Ortega, and I. G. Mikellides, “Facility Effect Characterization Test of NASA’s HERMeS

Hall Thruster,” in *52nd AIAA/SAE/ASEE Joint Propulsion Conference* (American Institute of Aeronautics and Astronautics, 2016).

⁵J. A. Walker, J. D. Frieman, M. L. Walker, V. Khayms, D. King, and P. Y. Peterson, “Electrical facility effects on Hall-effect-thruster cathode coupling: Discharge oscillations and facility coupling,” *Journal of Propulsion and Power* **32**, 844–855 (2016).

TABLE B.1: Training error metrics of the intermediate model and the model of the present work. Symbols have the same meanings as in Tab. VI

QoI	ξ [%]	Distribution	μ_{50}	μ	σ	μ_{50}/ξ
V_{cc} [V]	1	Posterior (old model)	2.6	2.6	0.1	2.6
		Posterior (new model)	2.5	2.7	0.5	2.5
T_c [mN]	1	Posterior (old model)	11.4	11.2	0.4	11.4
		Posterior (new model)	3.3	3.5	0.5	3.3
I_D [A]	10	Posterior (old model)	37.6	38	0.5	3.8
		Posterior (new model)	3.3	3.9	1.4	0.3
u_{ion} [m/s]	5	Posterior (old model)	13.8	16.6	0.5	2.8
		Posterior (new model)	12.2	13.8	1.2	2.4
j_{ion} [A/m ²]	20	Posterior (old model)	34.7	33	0.4	1.7
		Posterior (new model)	11.4	18.7	1	0.6

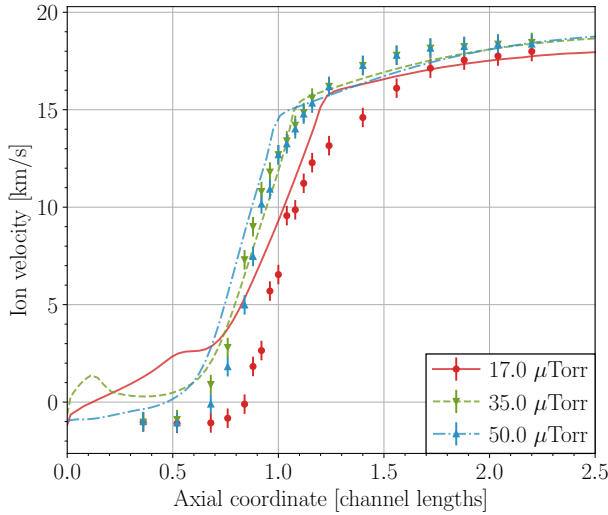


FIG. B.2: Ion velocity profiles for the SPT-100 at different background pressures using the model of Ref. 10.

- ⁶R. Hofer, I. Katz, D. Goebel, K. Jameson, R. Sullivan, L. Johnson, and I. Mikellides, “Efficacy of Electron Mobility Models in Hybrid-PIC Hall Thruster Simulations,” in *44th AIAA/ASME/SAE/ASEE Joint Propulsion Conference & Exhibit* (American Institute of Aeronautics and Astronautics, 2008).
- ⁷I. G. Mikellides and A. L. Ortega, “Challenges in the development and verification of first-principles models in Hall-effect thruster simulations that are based on anomalous resistivity and generalized ohm’s law,” *Plasma Sources Science and Technology* **28**, 14003 (2019).
- ⁸A. L. Ortega, I. G. Mikellides, V. H. Chaplin, J. S. Snyder, and G. Lenguito, “Facility pressure effects on a Hall thruster with an external cathode, I: Numerical simulations,” *Plasma Sources Science and Technology* **29**, 035011 (2020).
- ⁹T. A. Marks and B. A. Jorns, “Challenges with the self-consistent implementation of closure models for anomalous electron transport in fluid simulations of Hall thrusters,” *Plasma Sources Science and Technology* **32**, 045016 (2023).

- ¹⁰J. D. Eckels, T. A. Marks, M. G. Allen, B. A. Jorns, and A. A. Gorodetsky, “Hall thruster model improvement by multidisciplinary uncertainty quantification,” *Journal of Electric Propulsion* **3** (2024), 10.1007/s44205-024-00079-w.
- ¹¹M. L. R. Walker, D. Lev, M. Saeedifard, B. A. Jorns, J. Foster, A. D. Gallimore, A. A. Gorodetsky, J. L. Rovey, H. B. Chew, D. Levin, J. D. Williams, A. Yalin, R. E. Wirz, J. Marian, I. Boyd, K. Hara, and K. Lemmer, “Overview of the Joint Advanced Propulsion Institute (JANUS),” in *Proc. of the 37th International Electric Propulsion Conference* (2022) IEPC-2022-156.
- ¹²B. A. Jorns and M. P. Byrne, “Model for the dependence of cathode voltage in a Hall thruster on facility pressure,” *Plasma Sources Science and Technology* **30**, 015012 (2021).
- ¹³T. Marks, P. Schedler, and B. Jorns, “HallThruster.jl: A Julia package for 1D Hall thruster discharge simulation,” *Journal of Open Source Software* **8**, 4672 (2023).
- ¹⁴M. G. Allen, J. D. Eckels, M. P. Byrne, A. A. Gorodetsky, and B. A. Jorns, “Application of Optimal Experimental Design to Characterize Pressure Related Facility Effects in a Hall Thruster,” in *Proc. of the 37th International Electric Propulsion Conference* (2022).
- ¹⁵R. Sahu, A. R. Mansour, and K. Hara, “Full fluid moment model for low temperature magnetized plasmas,” *Physics of Plasmas* **27**, 113505 (2020).
- ¹⁶N. Macdonald, Q. Pratt, M. Nakles, N. Pilgram, M. Holmes, and W. Hargus, “Background Pressure Effects on Ion Velocity Distributions in an SPT-100 Hall Thruster,” *Journal of Propulsion and Power* **35**, 1–10 (2019).
- ¹⁷J. Sankovic, J. Hamley, and T. Haag, “Performance evaluation of the Russian SPT-100 thruster at NASA LeRC,” in *23rd International Electric Propulsion Conference* (1993).
- ¹⁸J. D. Frieman, T. M. Liu, and M. L. R. Walker, “Background Flow Model of Hall Thruster Neutral Ingestion,” *Journal of Propulsion and Power* **33**, 1087–1101 (2017).
- ¹⁹D. L. Brown, M. L. R. Walker, J. Szabo, W. Huang, and J. E. Foster, “Recommended practice for use of faraday probes in electric propulsion testing,” *AIAA Journal of Propulsion and Power* **33** (2017), 10.2514/1.B35696.
- ²⁰R. R. Hofer, S. E. Cusson, R. R. Lobbia, and A. D. Gallimore, “The H9 magnetically shielded Hall thruster,” in *35th International Electric Propulsion Conference, Atlanta, Georgia, USA* (2017) IEPC-2017-232.
- ²¹K. D. Diamant, R. Liang, and R. L. Corey, “The Effect of Background Pressure on SPT-100 Hall Thruster Performance,” in *50th AIAA/ASME/SAE/ASEE Joint Propulsion Conference, AIAA Propulsion and Energy Forum* (American Institute of Aeronautics and Astronautics, 2014).

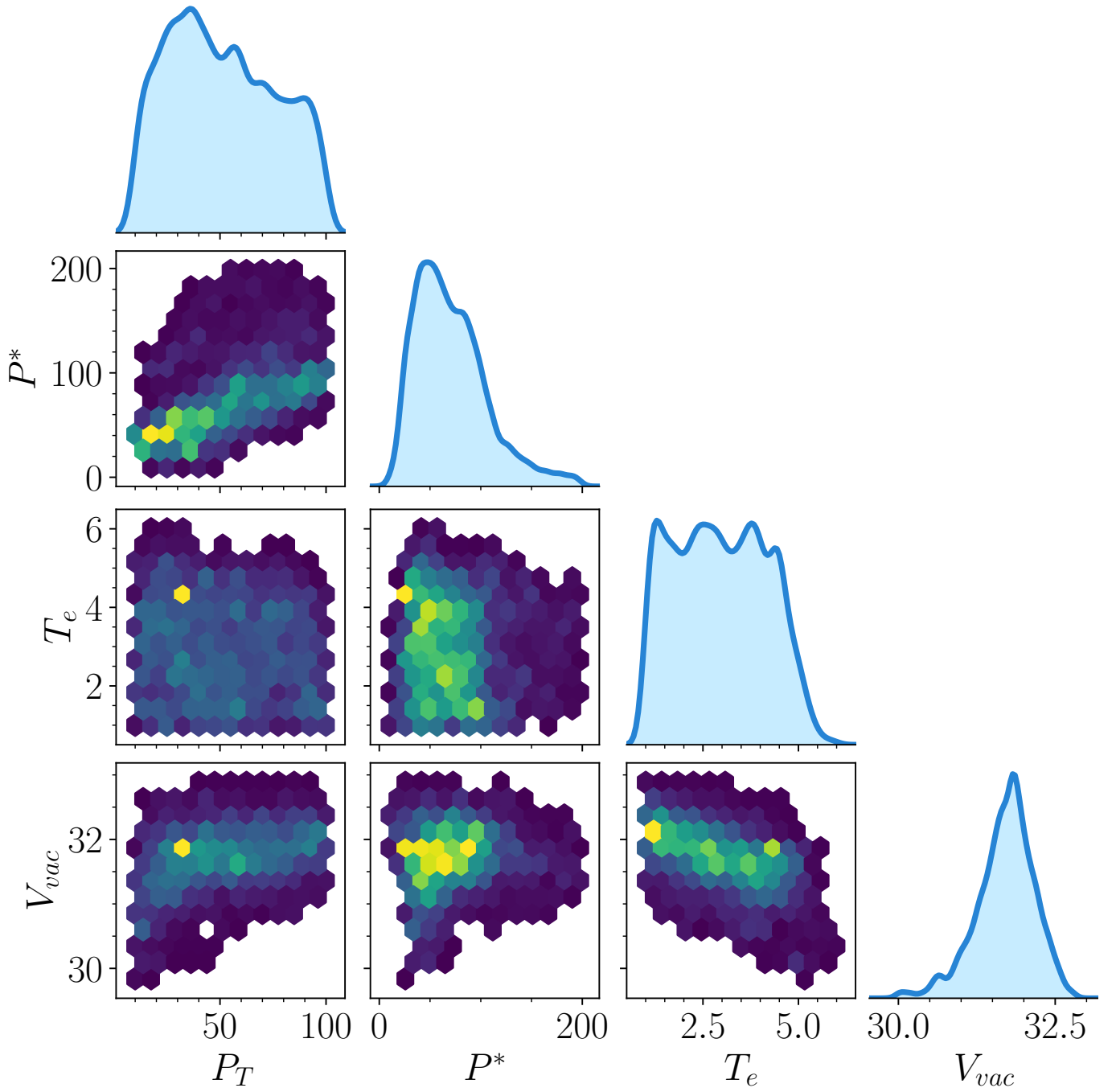


FIG. C.1: 1-D and 2-D marginal posterior distributions for the SPT-100 cathode parameters.

²²M. G. Allen, P. J. Roberts, and B. A. Jorns, “Direct measurements of the pressure dependence of the electron temperature in a magnetically shielded Hall thruster,” in *38th International Electric Propulsion Conference, Toulouse, France (2024)* IEPC-2024-821.

²³M. G. Allen, W. Hurley, A. Eckhaus, D. Brick, J. Cabrera, C. Lipscomb, M. Walker, and B. Jorns, “A pressure study on a 9kw-class magnetically shielded hall Effect thruster across facilities,” in *39th International Electric Propulsion Conference (2025)* IEPC-2025-708.

²⁴J. D. Cabrera, D. Lev, M. L. R. Walker, M. Allen, B. A. Jorns, A. Thomas, K. M. Lemmer, S. Clark, R. Thompson, J. L. Rovey,

R. Cowan, L. Franz, C. Cretel, S. Biswas, R. E. Wirz, E. Ku, S. Thompson, J. D. Williams, T. Topham, J. E. Foster, J. Stienike, and A. P. Yalin, “Overview of the Joint Advanced Propulsion Institute (JANUS) Facility Interpolation Test,” in *39th International Electric Propulsion Conference, London, England (2025)* IEPC-2025-615.

²⁵H. Haario, M. Laine, A. Mira, and E. Saksman, “DRAM: Efficient adaptive MCMC,” *Statistics and Computing* **16**, 339–354 (2006).

²⁶A. L. Ortega, B. Jorns, I. G. Mikellides, and R. R. Hofer, “Numerical simulations of the XR-5 Hall thruster for life assessment at different operating conditions,” in *51st AIAA/SAE/ASEE Joint Propulsion Conference (2018)*

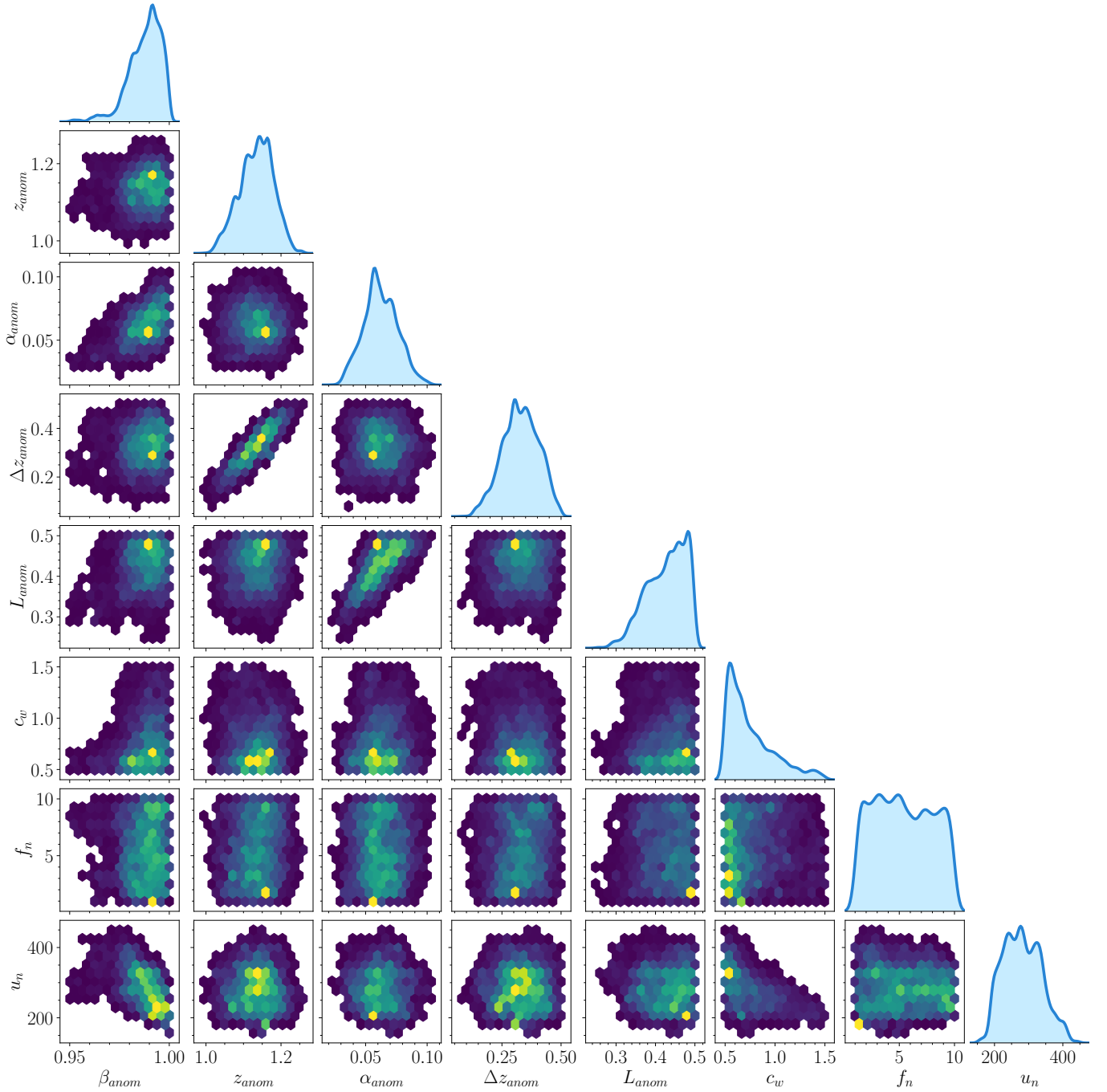


FIG. C.2: 1-D and 2-D marginal posterior distributions for the SPT-100 thruster parameters.

<https://arc.aiaa.org/doi/pdf/10.2514/6.2015-4008>.

- ²⁷K. Hara and I. G. Mikellides, “Characterization of low frequency ionization oscillations in hall thrusters using a one-dimensional fluid model,” in *2018 Joint Propulsion Conference, Cincinnati, Ohio, USA* (2018) AIAA 2018-4904.
- ²⁸I. G. Mikellides, A. L. Ortega, V. H. Chaplin, and J. S. Snyder, “Facility pressure effects on a Hall thruster with an external cathode, II: theoretical model of the thrust and the significance of azimuthal asymmetries in the cathode plasma,” *Plasma Sources Science and Technology* **29**, 035010 (2020).
- ²⁹P. J. Roberts and B. A. Jorns, “Inferring Electron Heat Flux in a High-Power Hall Thruster with Incoherent Thomson Scatter-

ing,” in *AIAA SCITECH 2024 Forum*, AIAA SciTech Forum (American Institute of Aeronautics and Astronautics, 2024).

- ³⁰K. Nishii and D. A. Levin, “Three-dimensional kinetic simulations of carbon backspattering in vacuum chambers from ion thruster plumes,” *Journal of Propulsion and Power* **40**, 123–137 (2024).
- ³¹C. P. Lipscomb, M. J. Stasiukevicius, I. D. Boyd, K. B. Hansson, T. A. Marks, B. D. G., and B. A. Jorns, “Evaluation of H9 Hall thruster plume simulations using coupled thruster and facility models,” in *38th International Electric Propulsion Conference, Toulouse, France* (2024) IEPC-2024-483.
- ³²M. P. Byrne and B. A. Jorns, “Data-driven models for the effects of background pressure on the operation of Hall thrusters,” in *36th*

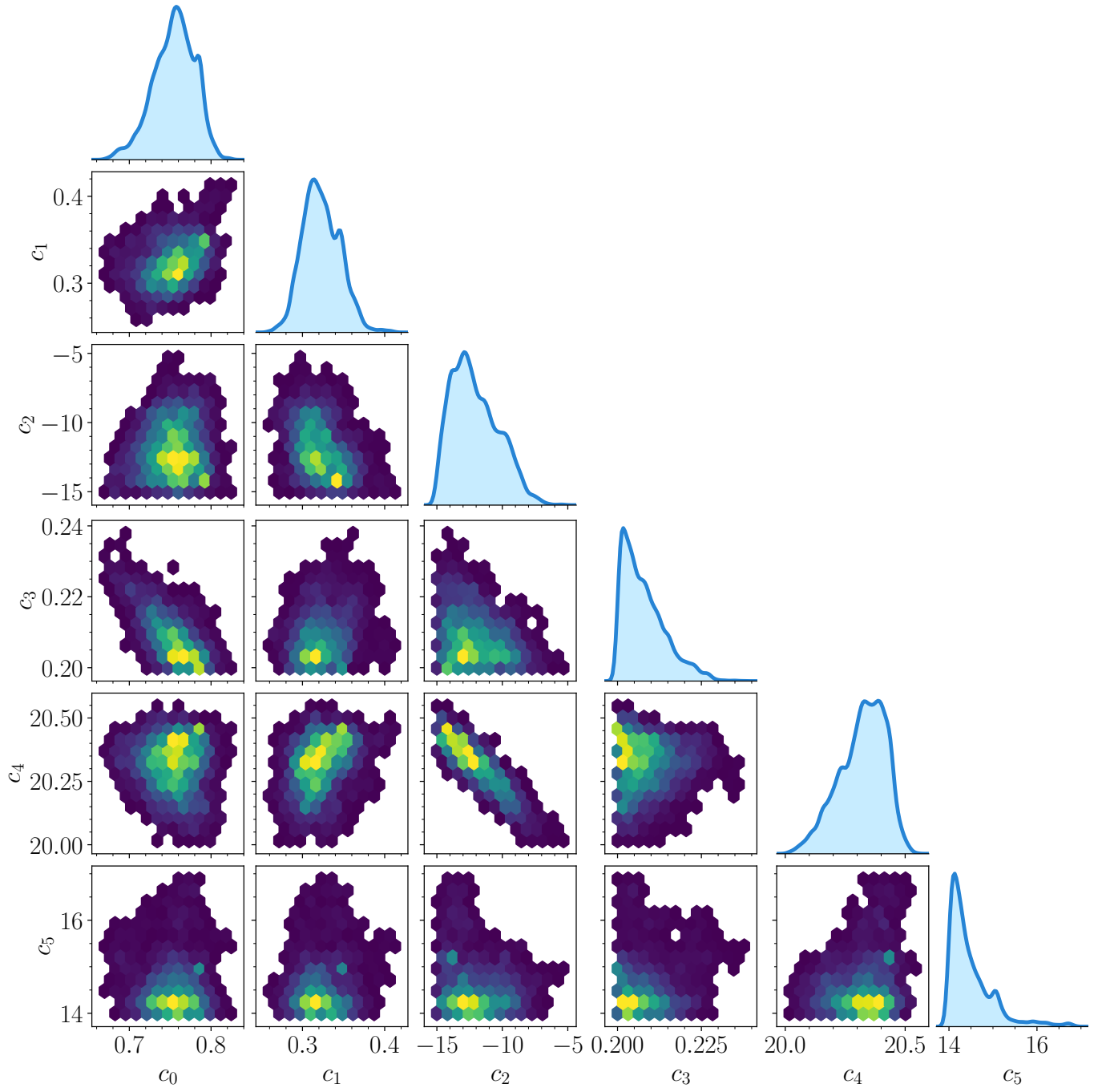


FIG. C.3: 1-D and 2-D marginal posterior distributions for the SPT-100 plume parameters.

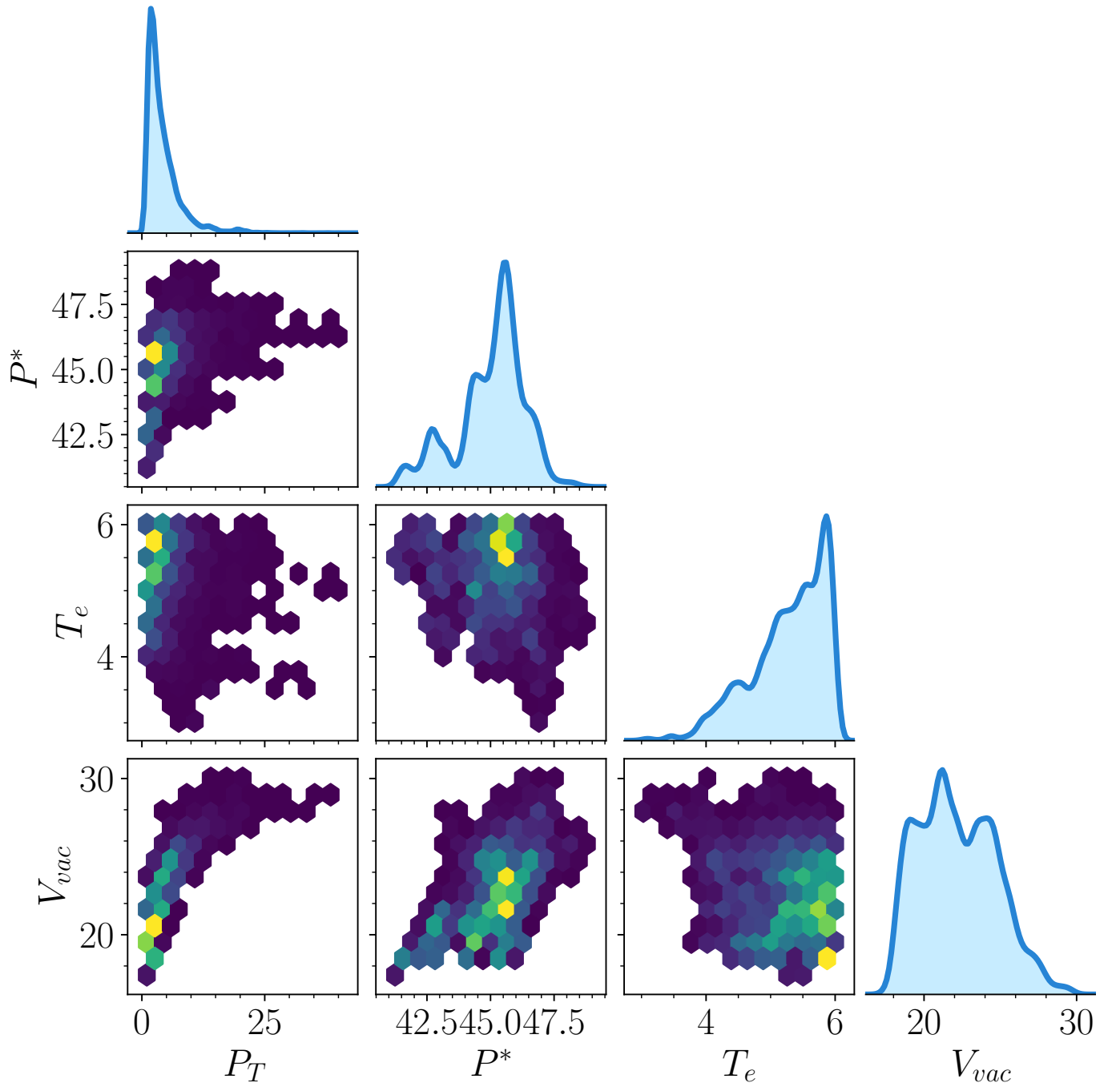


FIG. C.4: 1-D and 2-D marginal posterior distributions for the H9 cathode parameters.

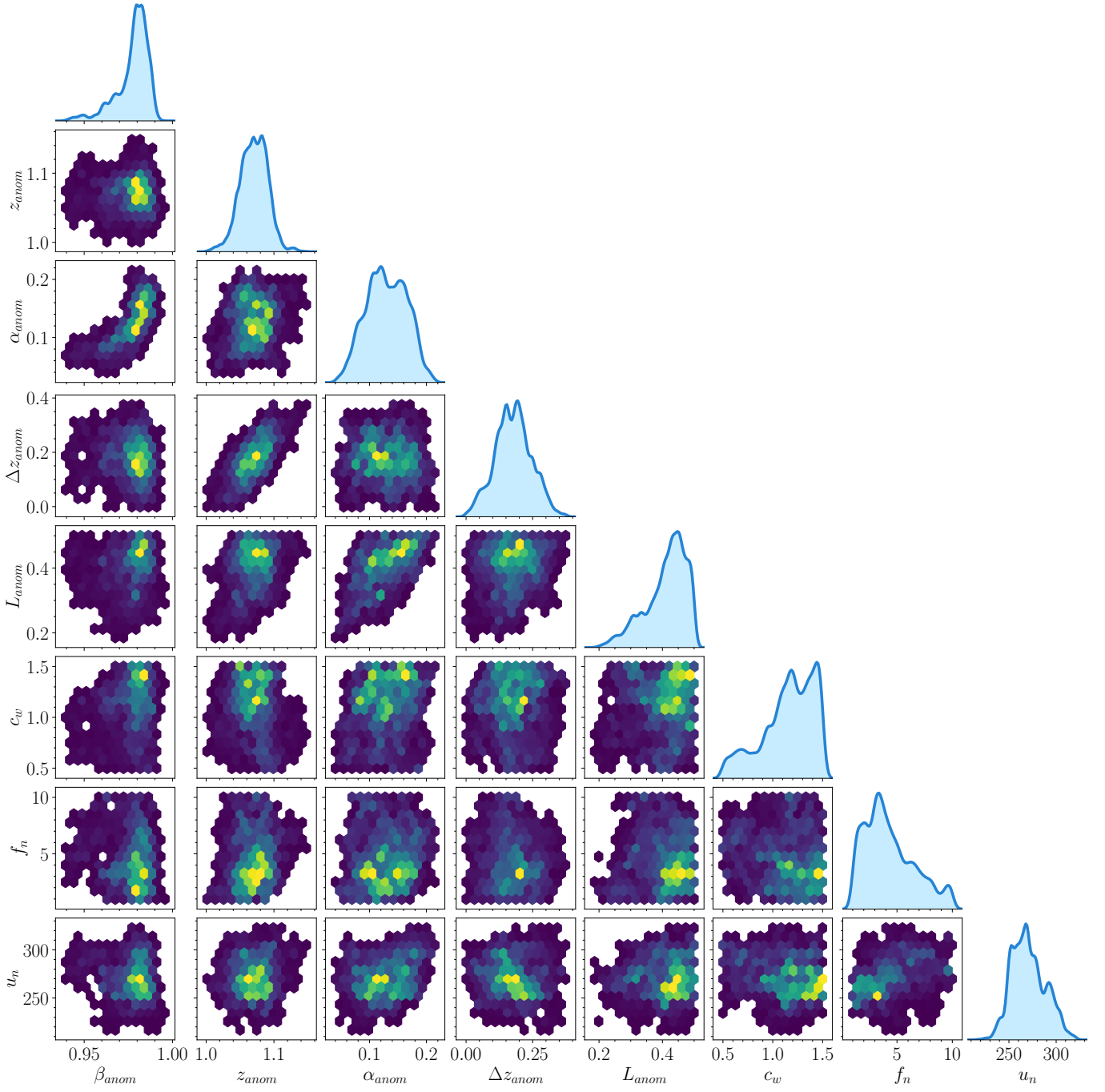


FIG. C.5: 1-D and 2-D marginal posterior distributions for the H9 thruster parameters.

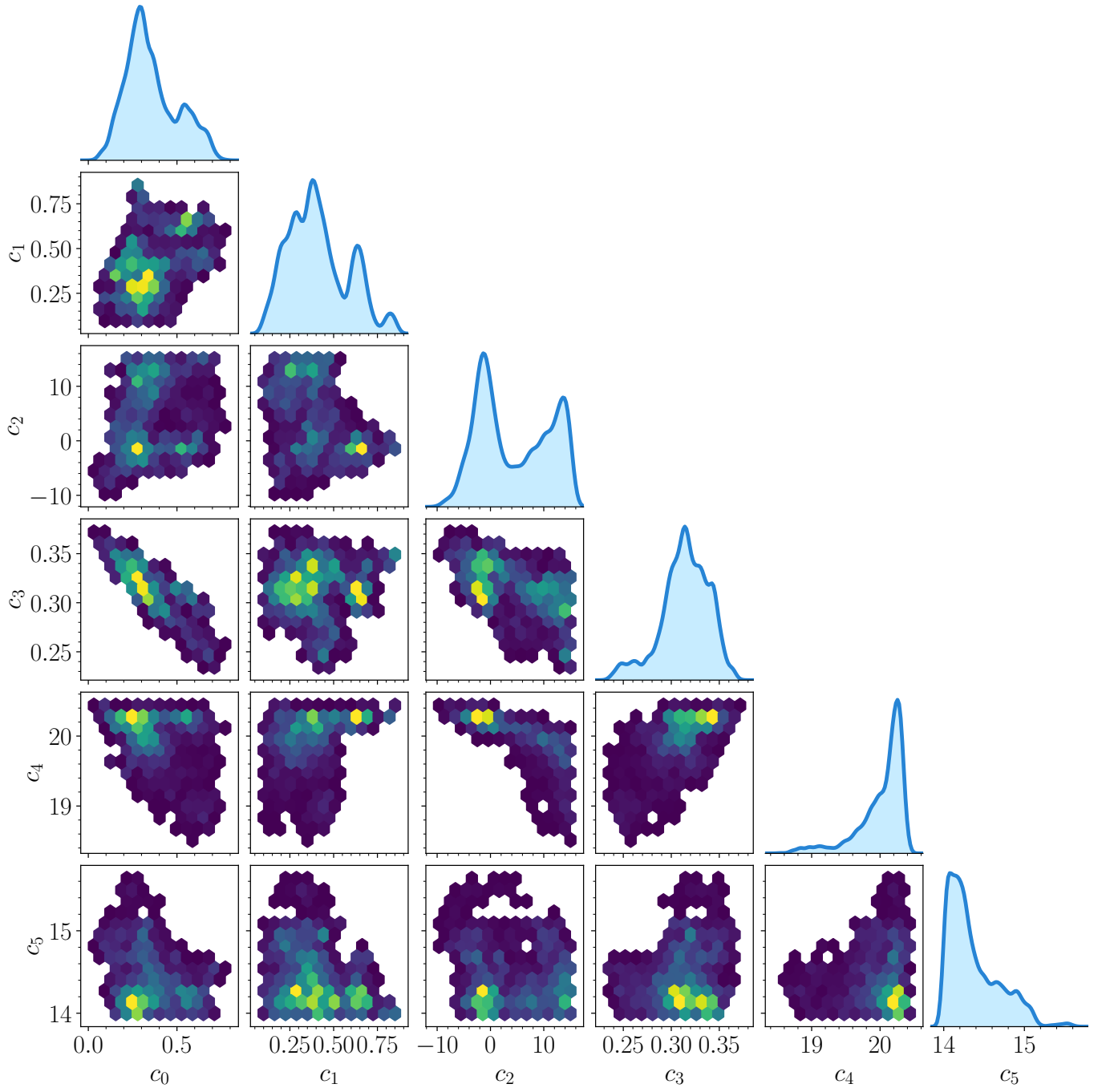


FIG. C.6: 1-D and 2-D marginal posterior distributions for the H9 plume parameters.